

# Current Opinion in Solid State and Materials Science

journal homepage: [www.elsevier.com/locate/cossms](http://www.elsevier.com/locate/cossms)

## Recent advances in 3D printing of porous ceramics: A review

Lim Chin Hwa <sup>a,b</sup>, Srithar Rajoo <sup>a,b</sup>, Alias Mohd Noor <sup>a,b</sup>, Norhayati Ahmad <sup>b</sup>, M.B. Uday <sup>a,b,\*</sup><sup>a</sup> UTM Centre for Low Carbon Transport in Cooperation with Imperial College London, Institute for Vehicle Systems and Engineering, Universiti Teknologi Malaysia, 81310 UTM Skudai, Johor, Malaysia<sup>b</sup> Faculty of Mechanical Engineering, Universiti Teknologi Malaysia (UTM), 81310 Johor Bahru, Malaysia

### ARTICLE INFO

#### Article history:

Received 27 October 2016

Revised 16 August 2017

Accepted 20 August 2017

Available online 9 September 2017

#### Keywords:

3D printing

Porous ceramic

Porosity

Particle size

Scaffold

Biomaterials

### ABSTRACT

3D printing, alongside the rapidly advancing field of porous ceramics, is quickly expanding the horizon of what is going to be possible in the future. In this paper, 3D printing technology is evaluated for its compatibility with porous ceramic materials, due to its competitive process in terms of speed and specific tooling, especially for good quality fabrication. The paper reviews the capabilities of these new technology techniques for the fabrication of porous ceramic. The basic technology is the 3D printing techniques, which are used to fabricate porous green ceramic parts that are later sintered. Different ceramic materials are evaluated and the classification of different powders according to their 3D printing quality as well as material aspects is examined. The evaluation of 3D printing process in terms of the powders' physical properties such as particle size, flowability and wettability is also discussed. The relationship between the different 3D printing parameters and the final printing outcome are assessed.

© 2017 Elsevier Ltd. All rights reserved.

## 1. Introduction

Three-dimensional printing (3D printing) is a highly customizable technology, which is changing the ways to approach the problem of porous ceramic fabrication. The applications include customized surgical tools, patient specific prostheses, scaffolds, dental porcelain and porous ceramic filter fabrication [1–3]. 3D printing can be defined as a layer upon layer fabrication technology using material deposition in order to build up different geometrical shape of 3D components [3–5]. It is becoming known as direct digital fabrication, which uses CAD software to exactly determine how each layer will be constructed and prints objects through fusing a variety of materials (powder and binder, in the case of 3D ceramic printing) [6,7]. In this technique, a model is printed in a build platform that is filled with powder material. The liquid binder is applied through an inkjet printer head to the appropriate layer and solidifies the powder. The build platform is then lowered by 0.1 mm and another powder layer is spread over the first, and the process is repeated until the part is complete within the powder bed [2,8].

The microstructure features, such as porosity and pore size distribution are very important factors for various potential applica-

tions of porous ceramics. Porous ceramics with different porous morphology and size distribution can be fabricated by different methods, for example, burning out a polymeric sponge impregnated with a ceramic slurry, solid state sintering, a sol-gel process, replication of polymer foams by impregnation, and gelcasting processes [9]. Introducing the 3D printing technology for porous ceramics offers increased flexibility and speed, eliminates tooling constraints, requires only low cost investment and also enables sustainability of the fabrication process [10–14].

Conventional porous ceramic fabrication faces many challenges to fabricate a fully interconnected pore network in terms of the need for highly toxic organic solvents, incomplete removal of residual particles in the polymer matrix, irregularly shaped pores, insufficient interconnectivity of pores, and thin structures; these difficulties mean there is poor repeatability, it is time consuming, and needs a large labor force [15]. Some examples of conventional methods include fiber bonding, solvent casting and particulate leaching, membrane lamination, melt molding and gas foaming. Even by casting or molding, it is difficult to easily and independently control the porosity and pore size of the porous ceramic, besides their restrictions on shape control [16].

The promise of 3D printing is based on customized parts that are typically made to order in unique configurations and in very small quantities. The use of the internet further enhances the possibilities of design sharing and modifications; thus the porous ceramics can be printed anywhere. According to Seitz et al. [17], 3D printing is well suited to fabricate complex porous ceramic

\* Corresponding author at: UTM Centre for Low Carbon Transport in Cooperation with Imperial College London, Institute for Vehicle Systems and Engineering, Universiti Teknologi Malaysia, 81310 UTM Skudai, Johor, Malaysia.

E-mail address: [ummb2008@gmail.com](mailto:ummb2008@gmail.com) (M.B. Uday).

## Nomenclature

$C_d$	cure depth	$\sigma_L$	liquid surface tension
$D_p$	light penetration depth	$\eta_L$	liquid dynamic viscosity
$E$	light irradiation dose	$V_\alpha$	volume of ethanol
$E_c$	critical energy	$V_\beta$	volume of ethanol vacuum forced into the pores of scaffold until no bubbles appeared
$\Delta P$	pressure loss	$V_\gamma$	remained volume of ethanol
$\mu$	dynamic viscosity	$P$	porosity
$L$	length of extruder	$l_z$	vertical pore size
$Q$	volumetric flow rate	$l_{xy}$	Horizontal pore size
$d$	nozzle diameter	$L_\alpha$	two adjacent distance between horizontal strand centers
$X_L^*$	weight fraction of large particles	$D$	diameter of the strand
$f_L$	large particles fractional packing density	$R$	pore radius
$f^*$	best composition of fractional packing density	$D_b$	pores distance
$f_s$	small particles fractional packing density	$P_N$	numbers of pores
$ff_\beta$	flow factor	$S_A$	bulk surface area
$\sigma_1$	consolidation stress	$S$	shape (circular or hexagonal)
$\sigma_2$	compression strength	$E_s$	compressive stiffness
$m$	absorbed liquid mass	$\sigma$	yield strength
$t$	time of Absorption	$C_1, C_2, n$	constants
$c$	capability constant		
$\rho_L$	liquid density		

matrices directly from powdered materials. Due to its capability for complexity, several studies have investigated the application of 3D printing for scaffold fabrication for tissue engineering [18–20].

Due to the enhancements in detail, precision and surface finish, 3D printing has been progressively used for such medical applications. Individual porous scaffold, which resembles natural bone structure, unique in size and shape, have recently been developed for use in 3D printing [21–23]. A study made by Zhange et al. [1], explored the feasibility of using a 3D printing process for a high accuracy fabrication of dental ceramic porcelain structures. However, the 3D printing process has a number of control parameters that can significantly affect the fabrication quality. In many cases, materials are supplied as powders and their characteristics such as particle size, shape and distribution will significantly influence the resulting structure and thus impact on the properties of the porous ceramic [24].

In 3D printing technology, larger ceramic particles are easily spread layer by layer. They have lower surface-volume ratio and larger pores, which results in the fabrication of more homogeneous ceramic parts. This is because the binders are able to form better bonding between particles inside the powder bed. On the other hand, finer ceramic particles produce thinner layers, lower surface roughness and promote printability [25]. Similarly to the microsintering process, thinner layers and correspondingly smaller particles sizes are required to achieve a finer matrix. 3D printing has demonstrated a good applicability for 3D microfabrication by taking advantage of the using of ceramic particles as a substrate in each layer [26]. Furthermore, advancements in the bonding between layers, dimensional stability, surface finish and resolution would be advantageous for 3D printed porous ceramics, especially in the micro- and nanofabrication fields.

A literature review by Campbell et al. [27] found that ceramic nanoparticle materials can lead to improvements in mechanical properties (tensile strength and modulus) of the final porous parts. Although there are a range of significant technical and scientific challenges to integrating the use of nanoparticles with 3D printing technology, this integration will enable their effective use for porous ceramics, especially for bone tissue engineering [28]. Different materials such as silica make the parts stiffer but brittle, whereas alumina can enhance the sintering characteristics.

As the overall, aim of this review is to explore 3D printing technology for its compatibility to print porous ceramics, the focus is on the 3D printing mechanism and its process to fabricate porous ceramics, as well as the applications, future trends and demand for high quality 3D printed porous ceramics. Parameters that can affect porous ceramics are also discussed, to characterize their performance further. A new approach to the design and fabrication of porous ceramics for tissue engineering using 3D printing is investigated, and also its biocompatibility and suitable mechanical properties for highly interconnected porous networks.

## 2. 3D printing technology processes

3D printing employs an additive manufacturing process in which the printer uses the ceramic powder which is deposited on a build platform and prints a geometrical model based on layer by layer fabrication technologies. It is a process of making three dimensional solid objects from a digital stereolithography file format (STL file). It builds up components from nothing, layer by layer, until the part is complete. Fig. 1 shows the graphical representation of the information in an STL file. The porous material on the left, was created in a CAD program and was subsequently saved as an STL file. The same material, on the right, is displayed triangulated, as the graphical information in the STL file. The spatial coordinates of the triangle vertices are contained in the STL file, and that information is transmitted to the printer for fabrication. A 3D printer device which presents a high number of triangles and vertices means that more data points were used to spatially define the part's surface, and thus increase the resolution of the printer device.

The 3D printing process is based on printing technology. It is a process which turns digital 3D models into solid objects by building the material layer by layer. Most commonly, 3D printing uses a powder-based method where solid particles are bound together by a binder material to generate a shape of part. The 3D printing process is illustrated in Fig. 2. The powder is generally distributed evenly onto the build platform by a powder-spreading roller. A liquid binder is deposited onto the powder layer, using a printer head. Whenever the liquid binder is applied to the powder, the particles are joined together. After the first layer is completed, the build

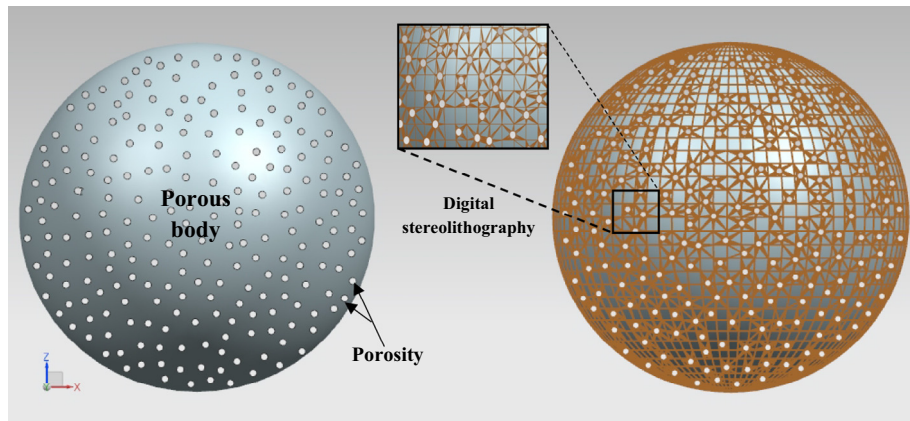


**Fig. 1.** Graphic representation of information in an STL file. [29].

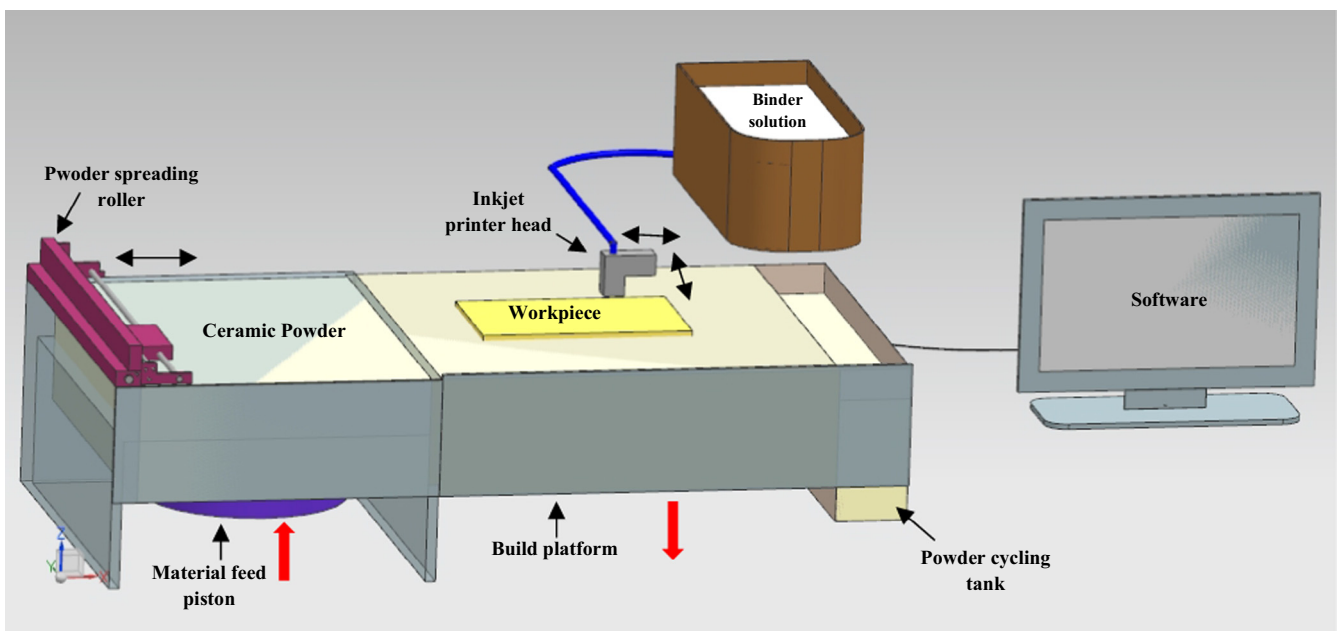


**Fig. 2.** The 3D printing process schematic diagram [8].

platform is then lowered and another powder layer is spread over the previous layer and the binder is deposited again over the new surface layer. The excess powder is being rolled into the powder recycling tank to be recycled and reused. The process is repeated until the whole part is completed within the build platform. After completion, the build platform is raised and the green part is brushed away from the loose powder which serves as support material during the 3D printing process [8]. Thus, this technology is able to print complex shapes, because the powder completely surrounds and supports the parts printed during each step.

A variety of 3D printing techniques have been used to create porous ceramic parts including Stereolithography (SLA), Selective Laser Sintering (SLS), Selective Laser Melting (SLM), Fused Deposition Modeling (FDM) and Binder based 3D printing (3DP). These techniques are differentiated by the manner of fabrication. For SLA, a 3D component is built slice by slice from bottom to top in a liquid polymer that is hardened upon exposure to radiation from a UV laser. Griffith and Halloran [30], addressed direct fabrication of 3D complex ceramic parts by replacing a resin-based system with a ceramic suspension-based system. They prepared a ceramic suspension for dispersing various types of ceramic materials,

including alumina, silica and zirconia, in both aqueous and non-aqueous liquid media. Due to the use of the ceramic suspension, the SLA process has been called ceramic stereolithography (Cer-SLA). To build the 3D component, CerSLA uses thin liquid layers of ceramic monomer suspension, which are solidified by an ultra-violet (UV) laser through the photo-polymerization mechanism.

Instead of using a UV laser, SLS and SLM apply sintering and melting techniques respectively, through a laser. SLM is a process that uses the laser to melt the powder particles and causes the particles to fuse together, whereas SLS makes the particles compact together without melting [31]. As a result, both processes are capable of producing 3D components with good mechanical properties and low porosity. A study has also shown that SLM can offer the possibility of manufacturing complex, high density, high strength and net-shaped ceramics with an appropriate preheating process [32].

In FDM, the filament can be made with a mixture between ceramic and binder and is extruded through a nozzle that traces the cross sectional geometry of the part, layer by layer. The latest FDM system includes two nozzles, one for the part material and another one for the support material. The filament is curled into

a coil for portability and fed into a hot nozzle to produce the desired shape. This is the most common technique, due to its simplicity and low cost [33]. However, the ceramics are limited to those with high melting temperature, thus resulting in difficulty in fused deposition [34]. Factors to be considered in FDM are the necessity for a steady nozzle speed, material extrusion rate, the support structure and the speed of the head, which all influence the overall layer thickness.

Different studies have shown that the suspension of ceramic powder can be printed by using a deskjet printer, after modifications. These studies used  $\text{Al}_2\text{O}_3/\text{CuO}$  [35],  $\text{ZrO}_2$  [36],  $\text{Ti}_3\text{SiC}_2$  [37] or  $\text{TiAl}_3/\text{Al}_2\text{O}_3$  [38] to fabricate complex-shaped ceramic objects. In this binder-based 3D printing, ceramics were suspended in a liquid binder to form the shapes. The liquid binder is locally applied on a powder layer and forms the bonding between powder particles. The polymeric binders are dropped onto the ceramic powder bed surface and subsequently form a cross section of the part [39]. However, the 3D printed ceramic components were found to have a large sintered shrinkage rate due to their low density. Thus, it is desirable to improve the density of the 3D printed ceramic component in order to control the dimensional accuracy. Zhao et al. [40] found that the relative density can be increased rapidly with the addition of binder content. In the 3D printing process of  $\text{ZrO}_2$  green bodies, a zirconia/polyvinyl alcohol (PVA) mixture was chosen as the precursor powder material, while the nano-zirconia suspension was used as a binder. Green bodies were sintered at 1400 °C for 2 h. According to their findings, if the binder content is increased from 50% to 125%, the relative density increases from 75.2% to 86.8%. The structure of the 3D printed green body is loose and porous, and the linear shrinkage of the sintered body is more than 30%. Thus, an increase in binder content would increase the relative density of the green bodies, and number of bonding bridges per unit volume of the sintered bodies and thus also decrease the linear sintered shrinkage. In addition, smaller linear shrinkage would improve the dimensional stability of the parts.

Among the different 3D printing techniques, the main considerations in choosing the 3D printing technology for porous ceramics are generally speed and cost of fabrication, materials selection, maximum resolution and accuracy, maximum dimensions of the porous part and minimum printing layer thickness [41]. Other criteria for assessment of each technique include surface quality, post-finishing, precision, resistance to impact, flexural strength, prototype cost and post cure, are shown in Table 1.

## 2.1. Stereolithography (SLA) technique

Stereolithography (SLA) is one of the 3D printing techniques used for creating 3D objects on a layer by layer basis using photopolymerization. It is also known as optical fabrication, solid

free form fabrication, solid imaging, photo-solidification and resin printing. It involves a process in which the concentrated beam of ultraviolet light causes curing of the molecule chains, starting from the bottom layer to the top layer, to create the 3D object. When the material is exposed to the concentrated light beam, it solidifies, one layer at a time, until all layers in the model are shaped. In addition to filling in regions not connected to the part, which causes material waste and post-processing to remove these fillings, there is a need for post-curing to improve the parts' finish [41].

Ceramic stereolithography (CerSLA) involves an ultraviolet (UV)-curable system which consists of polymerization of the ceramic particles' suspended in a photopolymer. However, there are some limitations to this technique, which include the poor difference of refractive index of the ceramic compounds with the organic structure being photosensitive and very poor absorption of the ceramic materials in the UV range. Indeed, the introduction of fine particles of ceramic (less than 1 μm) in a curable monomer presents a high degree of complexity, if compared with the classical formation of pure polymers. The scattering phenomenon of small ceramic particles will increase the processing time and also reduce the cure depth and dimensional resolution. For this UV curable monomer system, the uses of different additives such as dispersants into the ceramic powder help to stabilize the ceramic pastes, as well as inhibiting the agglomeration and settling of ceramic particles. Furthermore, the additives can also act as a thickening agent to support the ceramic part and provide high yield fabrication during the 3D printing system.

The ceramic particles are homogeneously suspended and photo-polymerised in the stereolithography resin to create polymer-ceramic composite objects [10,42–44]. The resin viscosity increases upon the addition of powder. Hinczewski et al. [45], reported that the maximum content of ceramic particles that could be achieved was around 53 wt%. Additionally, ceramic particle sizes smaller than the layer thickness were required during the fabrication process, to prepare the high accuracy 3D ceramic part. From their procedure, all ceramic parts have been fabricated by making the polymer-ceramic composite first, by SLA, followed by pyrolysis (polymer burn out) and finally sintering the ceramic part at high temperature [45–47].

With the help of CAD software, the UV laser is used to draw a pre-programmed design onto the material surface. The beam radiation is refracted by galvanometric mirrors to bond the subsequent layers and to harden the cross-sectional pattern. After that, it is transferred to a workbench in which one layer of thickness is continuously deposited and then the following layer, to continue the steps in fabrication. This fabrication process is repeated till the final ceramic part is completely built. The SLA process is illustrated in Fig. 3.

**Table 1**

Assessment criteria for each printing technique used for porous ceramic manufacture [41–45].

Techniques	SLA	SLS	SLM	FDM	3DP
Technique schematic					
Operating principle	Photo polymerization	Powder sintering	Powder melting	Melt extrusion	Powder + binder deposition
Characterizations	Average	Good	Poor	Average	Good
Surface quality	Average	Good	Average	Average	Good
Post-finish	Average	Good	Average	Average	Average
Accuracy	Excellent	Good	Poor	Average	Low
Resistance to impact	Average	Good	Good	Good	Medium
Flexural strength	Low	Excellent	Excellent	Excellent	No
Prototype cost	High	High	High	Low	Medium
Post cure	Yes	Yes	No	No	No

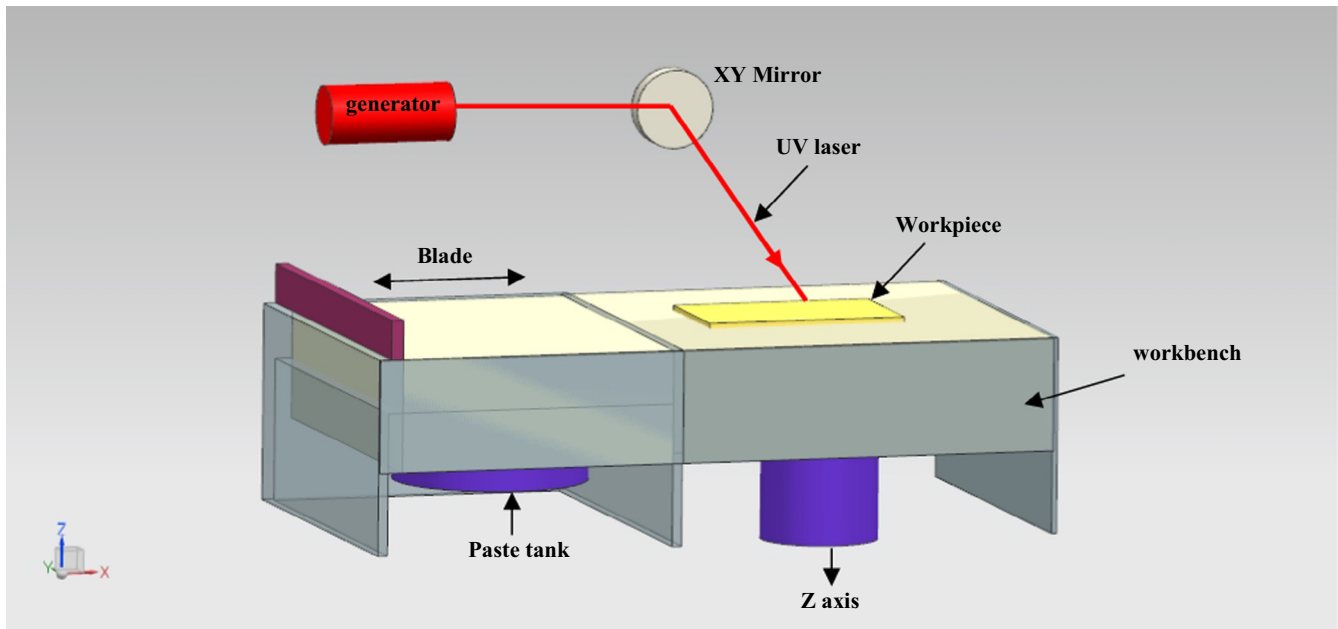


**Fig. 3.** SLA process: schematic diagram [48].

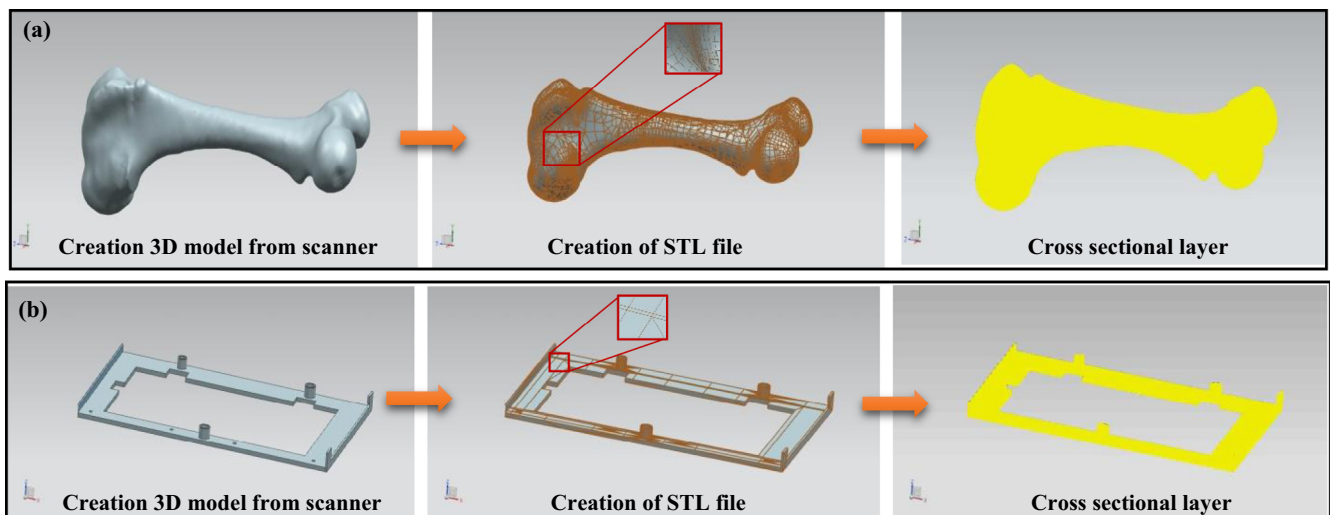


**Fig. 4.** Stereolithography ceramic part creation process. (a) Creation from 3D scanner. (b) Creation from CAD drawings [48].

The various stages for SLA are depicted in Fig. 4. First, the 3D component model can be obtained through scanner (Fig. 4a) or drawing (Fig. 4b). It generates the CAD data of the 3D component, which can be changed into STL file format. The STL format is the standard interface between 3D models of CAD software and a rapid prototyping system. It consists of closed triangular facets describing 3D CAD model surfaces. It is based on SLA to make fabricating and decomposes them to form layers of the cross-section, which also depends on conditions such as laser power, speed and build tracked patterns of the cross-section in each layer.

In SLA, control of the thickness of the layer being cured is essential. The amount of light energy to which the material surface is exposed is used to determine the cure depth. This energy can be controlled by adjusting the power of the light source, scan speed, or the time of exposure to light. This process involves different stages, which are initiation, propagation and termination. In practice, the kinetics of fabrication structures can be described

mathematically. A semi-empirical equation which represents the relationship between a solidified layer's thickness (the cure depth,  $C_d$  in  $\mu\text{m}$ ) and the amount of the light irradiation dose  $E$  ( $\text{mJ}/\text{cm}^2$ ) is used:

$$C_d = D_p \ln(E/E_c) \quad (1)$$

A plot of the determined depth of cure versus the applied irradiation dose is designated as a working curve [20]. The working curve is useful to control the right settings for SLA fabrication. The equation above, Eq. (1) is a modified form of the Beer-Lambert equation, which explains the exponential deterioration in focused light as it passes through the medium in which it is absorbed. In SLA, the time required for the material to achieve the gel point depends linearly on the concentration of light in that specific area. Thus, the depth to which the material is cured to the gel point,  $C_d$ , logarithmically increases with the dose of radiation applied,  $E$ , and time. For a specific SLA setup, the material can be

characterized by critical energy,  $E_c$  (mJ/cm<sup>2</sup>), and depth of penetration. A solidified layer can be formed from the material surface when the radiation dose,  $E$ , applied is above that necessary to achieve the gel point critical energy ( $E_c$ ). The  $E_c$  value depends on the concentrations of dissolved oxygen, photo-initiator and other inhibiting species. The light which penetrates into the material is directly related to the extinction coefficient of the Beer-Lambert equation, and is characterized by depth of penetration  $D_p$  [49].

To make sure of the mechanical and chemical bonds between the layers during fabrication, the conversion of macromers in the interface between the layers is higher than the gel point. Nevertheless, this over-exposure results in curing or partially curing into the preceding layer. The over-cure effect can be significant, particularly when preparing porous ceramic structures. Thus a polymer is used with a high extinction coefficient, compatible with low depth of light penetration,  $D_p$ , which will reduce the over-cure effect. In addition, the depth of light penetration can be decreased by including a dye in the polymer or increasing the photo-initiator concentration, because this inactive component competes with the photoinitiator to absorb light. However, if the depth of light penetration is decreased, this further increases the fabrication time.

SLA is particularly versatile in its application with regard to the freedom of design and the scales that can be built on the parts. With SLA, both sub-micron sized and decimeter sized structures can be made. In the biomedical field, these developments may bring benefit in the manufacturing of patient-specific models for molds to help template formation, tailor-made parts and complex surgical aids such as hearing devices [50,51]. In a project based on the study of implants, maxillofacial and craniofacial surgery. Chapat and Chartier [48], emphasize that it is vital that the ceramic implants are customized by SLA acquired with the 3D file directly from the scanner patient data. This technology provides a long-term, biologically active fabrication of the implant that can be adapted to the morphology of the patient so that the surgeon can meet the patient's requirements. The benefits are to reduce the period of hospitalization and save the patient's time. Ceramic porous structures are designed to improve bone growth and bone anchorage in the transplant process. These ceramic structures are directly included in the design of the implant before the fabrication of the 3D part.

Chu et al. [47] studied bone regeneration in the lower jaw of Yucatan minipigs using SLA to produce hydroxyapatite (HA) scaffolds with two different pore network architectures. The different scaffold designs presented significant variations with respect to the distribution, quantity and function of tissues that were created. The controlling of the geometry of the regenerated bone tissue was possible through the internal architectural design of the scaffolds. The architectural designs were generated through an image manipulation process. In the orthogonal design, bone and HA formed an interpenetrating matrix, whereas in the radial design, the regenerated bone formed an intact piece at the center of the implant. This indicates the importance of the pore architecture of the scaffold in bone formation. The total number of grids in the bone, void and soft tissue inside the implant pores were counted. The number of grids in the bone tissue were divided by the total number of grids to give the percent bone ingrowth inside the implants.

In another study, Zanchetta et al. [52] directly fabricated 3D high performance ceramics from preceramic poly-siloxanes. They claim that this is a versatile, simple and cost-effective procedure for fabricating accurate and precise ceramic microcomponents of different compositions. They used layer by layer selective curing of the photosensitive resin by Light Emitting Diode (LED) technology, according to a virtually sliced CAD model. The 3D ceramic microcomponents which were produced had a high density and were crack free, consisting of Si-O and Si-C bonds with no Si-Si

and C-O bonding through the pyrolysis of the cross-linked green body at 1000 °C. Thus, SLA also can also fabricate ceramic objects with a strength similar to that of conventionally produced components [53].

According to Chia et al. [54], SLA requires materials that have photocurable moieties such as resin with bioceramic dispersions for photo-crosslinking. In the applications of tissue engineering, very few biodegradable and biocompatible materials could be found that were dimensionally stable during photopolymerization. However, the advantages of SLA are the ability to create complex shapes with internal architecture and high resolution features, and ease the removal of unpolymerized resin [55]. The main disadvantages of SLA are the lack of a viable resin with appropriate characteristics for SLA treatment. Another drawback is that the use of radicals and photoinitiators may be cytotoxic over a long time period, due to the entrapment of residual unreacted monomer and photoinitiator, and the inability of SLA to create compositional gradients along the horizontal planes. Moreover, the use of photopolymerized resin may also lower the required mechanical properties for applications of hard tissue. It must be integrated into a temporary overload support (CAD) model, to make unsupported features, such as cantilevers and overhangs. The complete removal of excess temporary support is very difficult, because of the complex structure's shape.

The SLA system has been shown to be capable of processing a mixture of photopolymer resin such as 1,6-hexanediol diacrylate (HDDA) monomer with ceramic fillers [56]. The photopolymer resin can be subsequently removed to obtain a pure bioceramic scaffold [57]. The major advantage of using SLA is its ability to prepare a well-defined architecture. SLA can be used to fabricate scaffolds with strong support cell attachment. Scaffolds that are designed to be optimized for cell-delivery and mechanical properties for specific engineering applications can now be made. SLA is also useful to provide customized scaffolds with better surface finish.

For the advancement of this SLA technique, two-photon curing is increasingly used in SLA fabrication, especially to print a 3D microstructure. It is a technique using a short pulsed laser with a high peak power in order to achieve polymerization, since the quantum efficiency is quite low [55]. Two-photon curing is limited to 3D microfabrication from transparent resin, since the laser beam cannot be easily focused inside of a ceramic suspension. In the research by Zhang et al. [55], they successfully fabricated micro-gears, microtubes and micro convex cone structures with 3D complex shapes, high aspect ratio and a wide variety of functional materials. For the first time, ceramic microfabrication was successfully demonstrated.

In bilateral photon polymerization, there is an energetic initiation of the photon by absorption simultaneously from two photons, with a relatively low concentration. At the same time, the excitement gives enough energy to break the labile bond and initiate of the reaction of the treatment. Consequently, the two-photon process is a visual treatment of the non-linearity of relative treatment directly to the square rate to focus the laser, as in the case of a single photon-treatment. This will provide a local consumption of the treatment process and result in a higher resolution. High resolution for 200 nm can be achieved by using two-photon absorption in the SLA setup. A review of bilateral photon polymerization has been published by Lee et al. [58], and it was also the first application mentioned in a tissue engineering report in Weib et al. [59].

Interference lithography (holography) is another method for SLA that applies more than two light sources to create an interference pattern. Regular patterns with locally varying concentration of light can be obtained by light wave overlay [60]. This is useful for the creation of 3D photonic crystals, microframes, microsieves, micro- and nanostructures [61]. Holography provides a faster and

more accurate way of establishing patterns in photo-curable resin. Thus, it could be used to fabricate repetitive porous structures in tissue engineering.

SLA has become a strong prospective technique for biomedical engineering. It can be combined with medical imaging techniques such as Magnetic Resonance Imaging (MRI) and Computed Tomography (CT) for biomedical engineering purposes. It has been proven in practice to facilitate and improve the quality of surgical procedures, particularly complex surgical procedures, which position the implantation of specifically designed vital medical devices. The development of new resins has enabled biodegradable scaffolds to be used directly for tissue fabrication. Using hydrogels containing cells, peptide grafted structures, HA composites and modified natural resins, SLA has developed into a useful technique on a large scale, particularly for biomedical applications [62].

## 2.2. Selective Laser Sintering (SLS) and Selective Laser Melting (SLM) techniques

Laser-based 3D printing techniques have been rapidly growing and finding applications in various industries, including medical implants, automotive parts and aerospace parts with complex geometries and structures. However, the quality and process performance of 3D components have not yet met the industry levels in terms of dimensional accuracy, surface roughness, structural integrity, resultant mechanical properties and related processing times [63]. The techniques can be classified into SLS and SLM. SLS is a 3D printing technique that uses a laser as the power source to sinter powdered material to create a 3D component, whereas SLM uses a laser to fully melt the material rather than sintering it, thus allowing different properties in terms of crystal structure and porosity.

Selective Laser Sintering (SLS) is a method that applies the use of high energy lasers to selectively melt the thin layers of ceramic particles. In this process, a layer of powdered material is spread across a bed, where the laser moves across the bed, fusing the first layer together. The interaction between the powder and laser beam increases the temperature, thus inducing fusion between particles. Once completed, the bed is lowered and another layer of the material is spread across it and the process is repeated. This process is not restricted by the need for support material, because the support can be provided by the unbound powder [18,41,54]. It also

possible to produce layers that are 100 µm, 120 µm and 150 µm thick [64].

SLS is a layer-by-layer manufacturing process; thus, according to Vaezi et al. [25], smaller powder particle sizes and thin layers are required to achieve finer details. As shown in Fig. 5, an infrared system is used to heat the powdered material and the laser beam provides a subsequent sintering of the ceramic powder, locally. The depth of penetration of the laser beam energy to the bed of the ceramic powder is more than one layer, and layers are thus sintered together to subjacent layers. In the SLS process, two supply bins are situated to the left and right of the fabrication technique chamber to provide powdered material. Blasted fluidization by compressed gas inside the supply bins occurs gradually to prevent the aggregation of ceramic powders. The recoater is packed with ceramic on all end positions by a dosage notched roller, which determines the amount of ceramic powder. The building platform falls by one layer of thickness and is coated by the ceramic powder by moving the recoater from one side to another. There are two overflow bins to collect the excess material. The SLS process will be repeated layer by layer until the part is completed. The part is then removed from the powder bed [64].

SLS can produce complex ceramic structures, including 3D printing for bone tissue scaffold applications. This technique was used by Xia et al. [65] to fabricate scaffolds which showed a good biocompatibility and promotion of healing for bone defect. In their study, a novel biomimetic composite scaffold, known as nano-hydroxyapatite (HA)/poly-ε-caprolactone (PCL) was fabricated, with predesigned, well-ordered macropores and interconnected micropores. An example of internal porous architecture for a scaffold is illustrated in Fig. 6. Although the possibility of scaffolds fabricated by SLS has been developed, the method still presents some limitations, due to the high operating temperatures required during fabrication [54]. The binding of the particles requires a laser to scan the surface of the powdered particles and heat them to exceed the temperature transformation of glass. During the sintering, molecular diffusion on the outer surface along the length of the lead particles to form a neck between neighboring particles. Temporary excess support is not required, since the solid ceramic particles, unbound, are capable of supporting any cantilever structures. The sintering process does not involve complete melting of the ceramic powder, so the porosity of the original ceramic particles can be maintained [54].

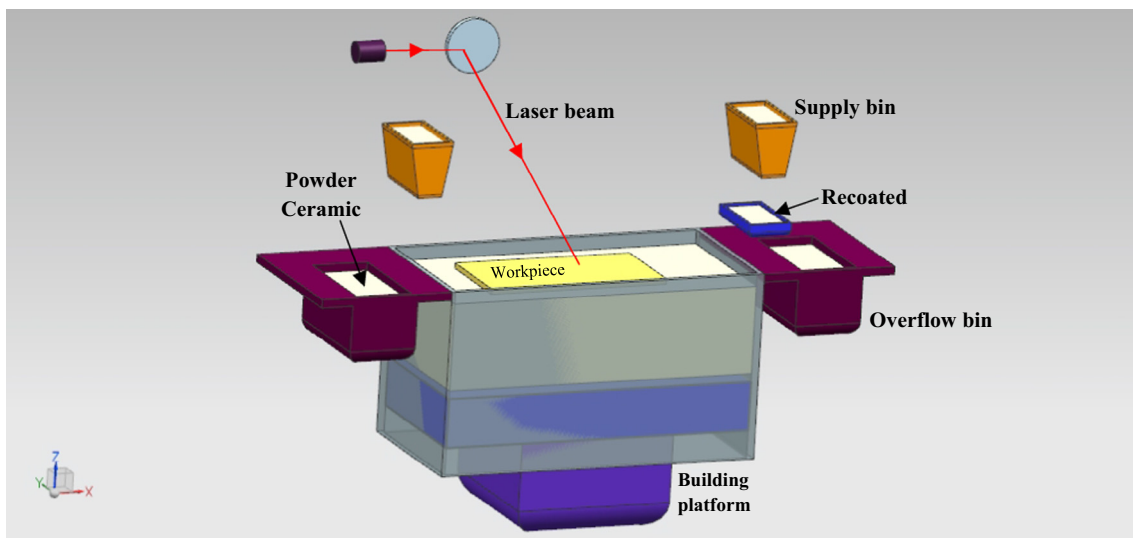


**Fig. 5.** Laser sintering process: schematic diagram [64].

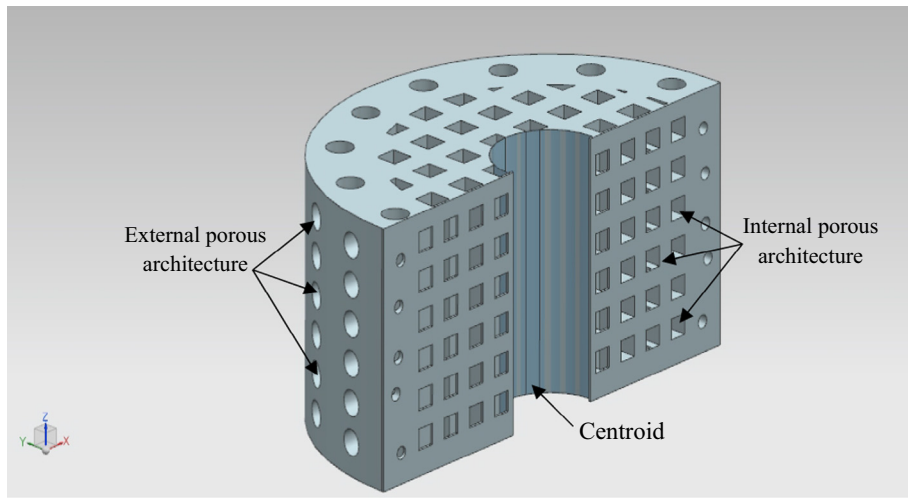


**Fig. 6.** The CAD scaffolds model used for SLS fabrication [54].

SLS requires intermediate binding materials such as thermoplastics (water soluble polyvinyl alcohol) for printing the ceramic components. This is because the ceramic powder has an excessively high melting point and high glass transition temperature. Thus, the ceramic powders are coated with polymer, which would melt first and fuse together. The bone implants have been fabricated by sintering calcium phosphate powder and polymer to achieve improve mechanical properties and bone regeneration potential [66,67]. The resulting application of focused laser and thermal energy induced sintering to take place, to produce porous implants. SLS processing of composites of bioresorbable polymers with inorganic osteoinductive materials such as tricalcium phosphate is capable of creating functional, tailored 3D implants incorporating gradients in both material composition and porosity. Thus, SLS is a very promising technique, especially for manufacturing tissue engineering scaffolds.

Beside the application for scaffold fabrication, Silva et al. [68] used SLS for prototype fabrication of a craniofacial skeleton with accuracy. The customized cranial implants were fabricated based on the digital images acquired from computerized tomography (CT) technology. CT technology provides better spatial resolution, good hard tissue contrast and relatively short imaging times [69]. A typical spatial resolution of CT is in the range of 400–600 µm, with slice thickness of less than 1 mm [70]. Tomographic images of a dry skull were manipulated with the biomedical software and the linear measurements were made on the models and compared with the corresponding dry skull measurements using an electronic caliper. They observed a dimensional error of 2.10% for this SLS fabrication. The models satisfactorily reproduced anatomic details, except for thin bones, small foramina and acute bone projections. The SLS prototypes showed greater dimensional precision and reproduced the craniomaxillary anatomy accurately. Fig. 7 shows the skull prototype fabrication and the dimensional measurements, which can be calculated as

$$\text{Mean absolute difference (mm)} = \text{prototype value} - \text{dry skull value} \quad (2)$$

$$\text{Mean relative difference (\%)} = \frac{(\text{prototype value} - \text{dry skull value}) \times 100}{\text{dry skull value}} \quad (3)$$

The selective laser melting (SLM) process is a 3D printing technique which is very similar to the SLS fabrication process. The SLM process uses higher power compared to the SLS process, thus

resulting in full melting of the ceramic powder and achieving high density functional parts [25]. In SLM (Fig. 8), a ceramic powder layer is deposited onto a substrate plate and selectively melted according to the CAD data. Subsequent lowering of the building platform, followed by additional powder deposition provides new material for a consecutive melting step [71]. The local heat is inputted by the focused laser causes large thermal gradients, accompanied by local stresses. As ceramics show little potential for plastic deformation, due to their covalent ionic bonding, these stresses may not be relieved, resulting in formation of micro-cracks. Employment of a high temperature preheating stage reduces the thermal gradients during laser processing and consequently crack formation may be avoided [32,72].

SLM uses high power to heat the ceramic powder above melting temperature to fuse the ceramic particles completely into a highly consolidated and dense structure. A connection between the neighboring and underlying layers can be achieved. The molten particles are attached to the surface and increase the roughness. Therefore, this surface structure usually requires post-machining. An approach by Hagedorn et al. [71], produced net-shaped parts with flexural strengths of above 500 MPa, without post-processing. They used a eutectic mixture of pure alumina ( $\text{Al}_2\text{O}_3$ ) and zirconia ( $\text{ZrO}_2$ ), which were completely molten, while crack formation was prevented by high temperature  $\text{CO}_2$  laser preheating. The eutectic material ratio exhibits a considerably lower melting temperature of 1860 °C, compared to the single phases (Fig. 9). Applications of this new technology comprise high-tech engineering ceramics, exploiting the possibilities of fabricating complex geometries for the medical, automotive or aerospace sectors.

The advantage of these techniques (SLS/SLM) is their capability to produce high fracture toughness and good mechanical properties useful for load-bearing application. However, not all the ceramics that fuse but do not decompose under the beam of laser Post-processing is required to remove excess ceramic particles. The diffusion and conduction of laser energy also cause unwanted fusion of neighboring ceramic powder, thus reducing the final resolution of the features. Moreover, the pore sizes using small ceramic particles are limited, as the creation of pores depends on the particle size of the ceramic powder used. Ceramic particles less than 5 µm in diameter will not be able to be used, due to poor spreading from clumping of the powder [54]. The SLM allows the fabrication of components with hollows and undercuts. Due to the design freedom, it is possible to individualize the components and to enlarge the number of variations arbitrarily. In SLM, the complexity of a component has a low effect on the unit costs. This

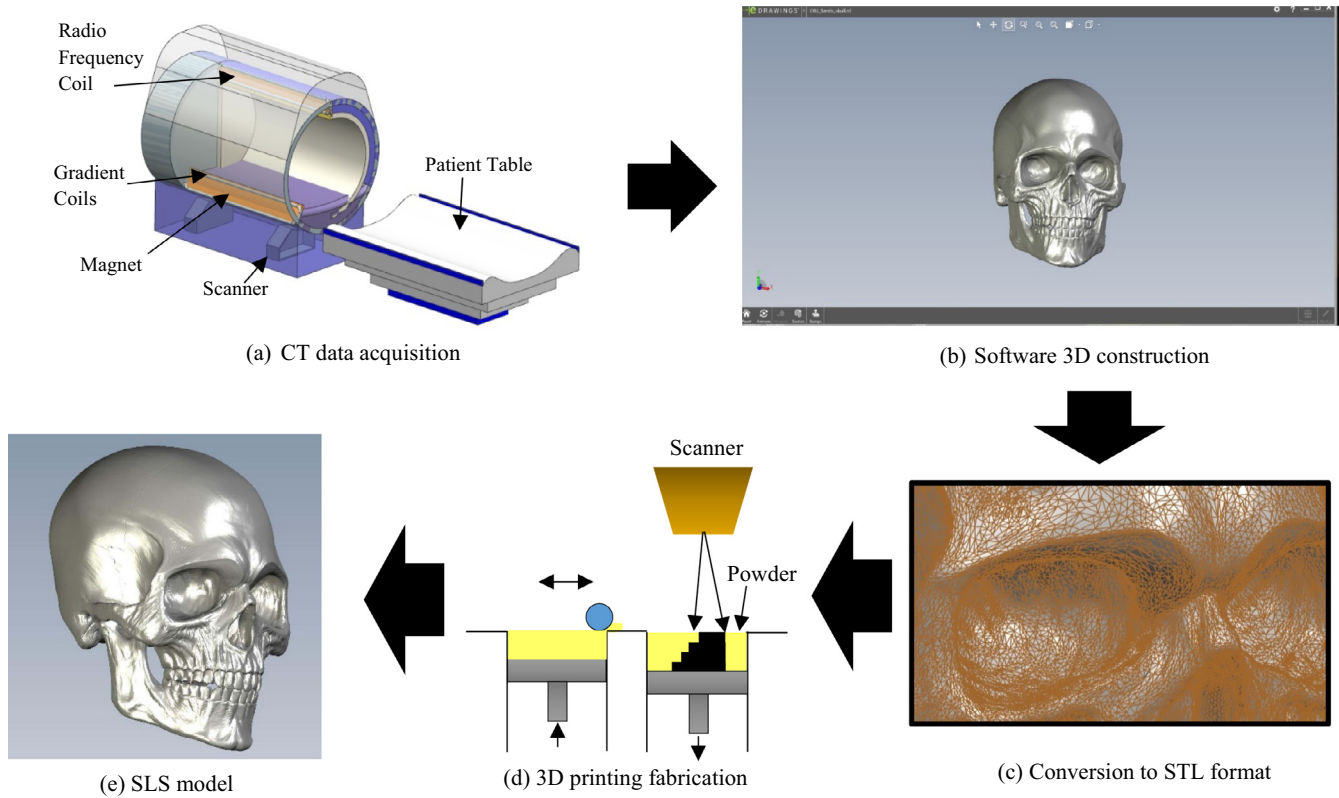


**Fig. 7.** Skull prototype fabrication and its mesh structure [68].

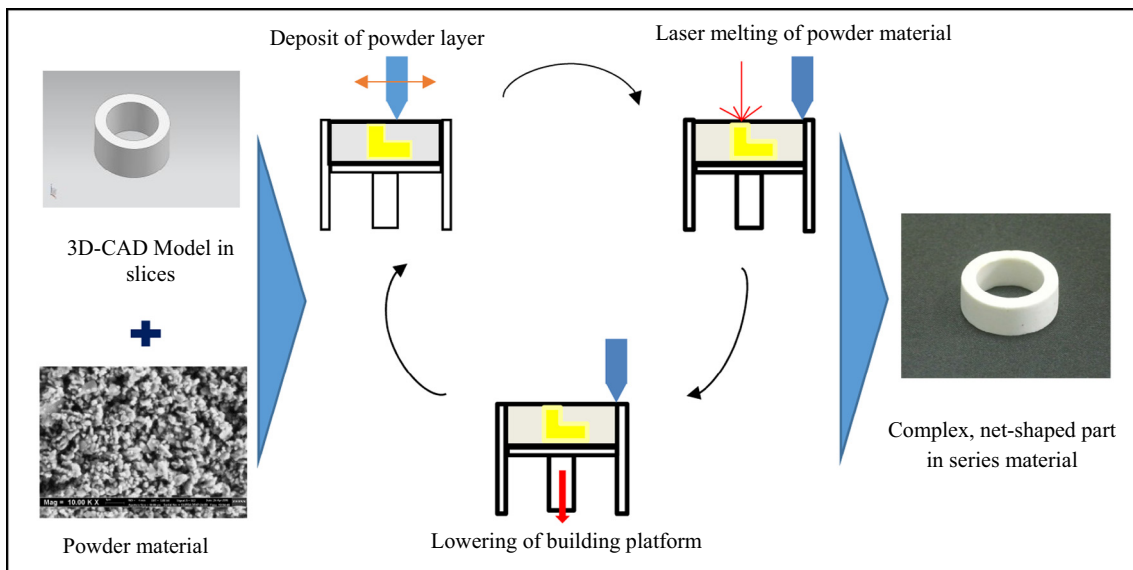


**Fig. 8.** Schematic illustration of the steps in SLM fabrication [71].

is because the costs of the SLM process are more volume- than geometrically-based. SLM provides parts with a high degree of complexity and low cost of fabrication, if compared with conventional methods.

### 2.3. Fused Deposition Modeling (FDM) technique

The Fused Deposition Modeling technique forms 3D objects from computer generated models, which can be derived from tomography scans, magnetic resonance imaging scans or CAD

model data. FDM is a technique that uses hot filaments which are selectively extruded from nozzles and then the layered 3D component is printed by moving the nozzles within the *x* and *y* axes [73]. The nozzles move according to the CAD drawing until the part is completed. FDM uses an extruder to discharge the filament material. It deposits the semi-molten material onto a platform in a layer by layer process ([Figs. 10 and 11](#)). The filament material is driven by two rollers. Once the first layer is completed, the base platform is lowered and the next layer is deposited. The 3D component is fabricated based on the accurate deposition of

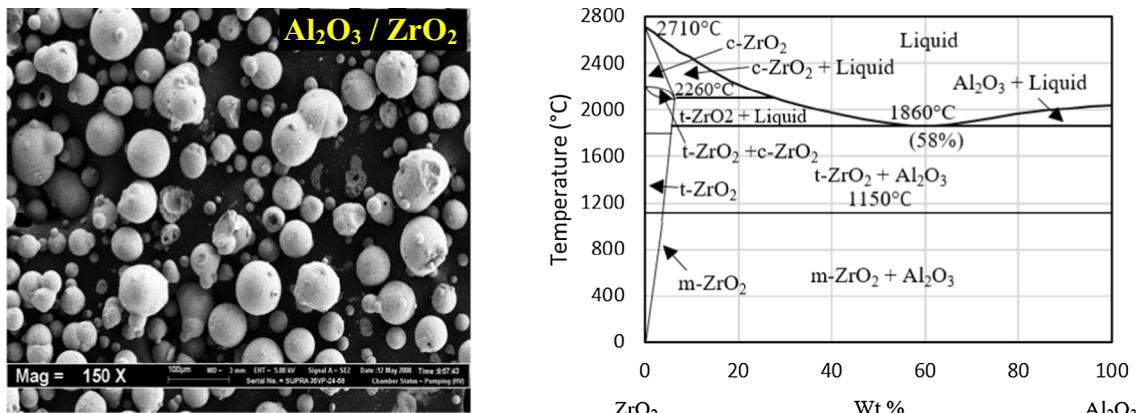


**Fig. 9.** (a) FESEM image of the dry mixed alumina/zirconia powder. (b) Phase diagram of the alumina and zirconia system.

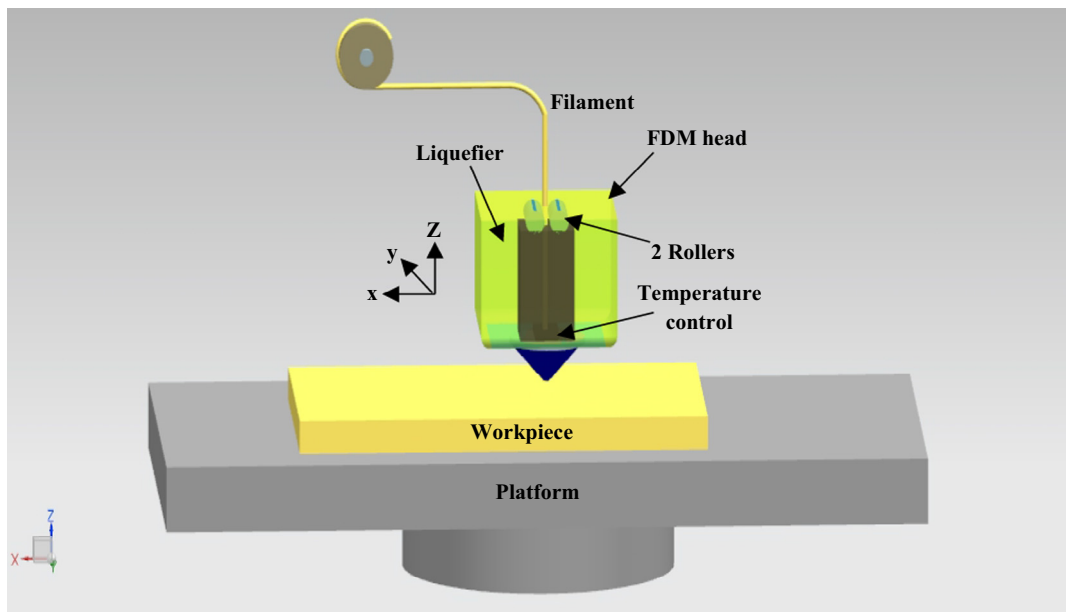


**Fig. 10.** FDM process schematic diagram [74].

thin layers from the extrudate. The processing parameters for filling each layer include the roller speed, the head speed, the slice interval, and the deposition direction within each layer [74].

Regarding its application, the FDM technique has been used previously to fabricate ceramic scaffolds [76]. The fabricated 3D scaffolds can have interconnected channel networks, high channel size and controllable porosity [74]. 3D porous ceramic parts made of layers of directionally aligned filaments by FDM have been obtained in the research of Onagoruwa et al. [77]. The porous ceramic bulk of fused silica was infiltrated mullite with aluminium metals to get composites of metal-ceramic. From this porous ceramic parts were successfully produced with minimal defects and good quality. The binder used for this technique was the polypropylene (PP) binder system. Another example using this technique was computed tomography (CT)-guided FDM, which was employed to fabricate polycaprolactone (PCL)/hydroxyapatite (HA) and PCL 3D artificial bones to mimic natural goat femurs [78]. The researchers propose several advantages which include easy producibility for manufacturers, good shaping ability and easy operability for surgeons. In addition, their work also suggests that PCL/HA 3D artificial bones could potentially be used to treat

load-bearing goat femur segmental bone defects and could benefit patients with bone repair needs.

An experiment by Tseng et al. [79] revealed that the porous structure of the scaffolds fabricated by the process of FDM depends on four key criteria. These include width of the road, thickness of slice, angle and gap raster. The width of road is the width of the extruded layer. Slice thickness is the thickness of the layer used to build a 3D component, while the raster angle is the angle between the horizontal raster and succeeding layers of the 3D component. The raster gap is the gap between the raster lines arranged within a sliced plane of the 3D component. Alteration of processing parameters allows for the fabrication of scaffolds with varying channel size and porosity. This research featured 3D scaffolds with fully interconnected channel networks, large channel size and controllable porosity [74].

Fused deposition of ceramics (FDC) is another term used in some literature sources which defines a modified FDM technique in which ceramic powder loaded with hot thermoplastics filaments is extruded [80–83]. During FDC, the thermoplastic resins melt, carrying the ceramic powders together. The ceramic parts contain 40–45 vol% binder in that formula. The ceramic parts are then

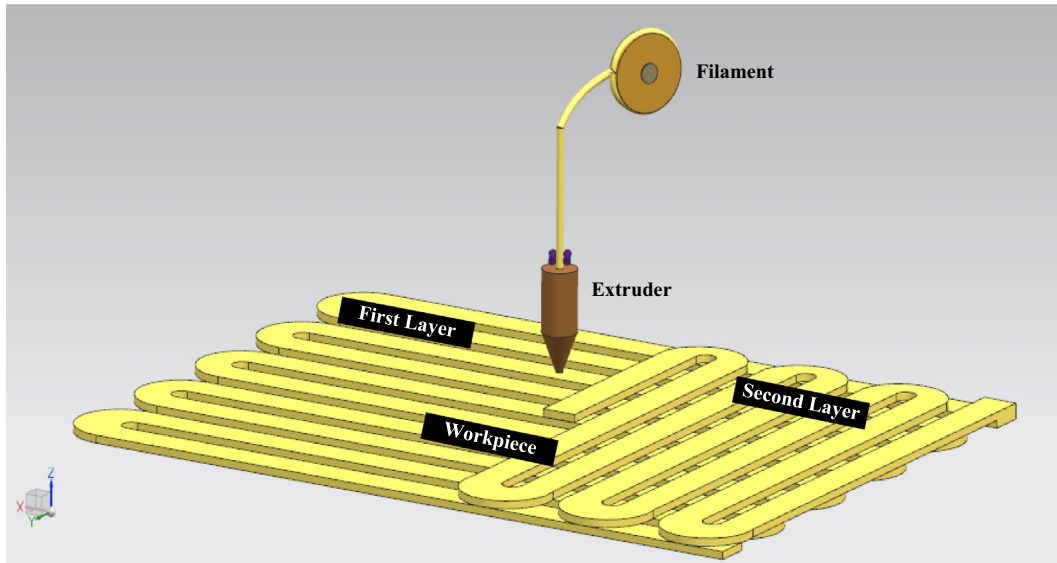


**Fig. 11.** Layer by layer process in FDM [75].

exposed to the removal of binder and the sintering cycle for densification. The FDC development process generally involves four stages, which are optimization of thermoplastic binder composition, fabrication of filament, process fabrication and, lastly, removal of binder and sintering program development.

In FDC, the basic necessities for feedstock filaments include low binder viscosity and high mechanical strength with high modulus and high strain. The low binder viscosity is to prevent the return flow of molten material. The high strength of the filament can serve as a piston throughout the fabrication, to prevent torsion. Good properties of the binder system and ceramic powders lead to good quality filament in FDC. The polymer binder system presents low viscosity requirement, high mechanical strength, high modulus, high strain and is easy to burn out, and also sufficient capacity to facilitate decomposition of the filaments and binder. Moreover, fine particles of ceramic powders with wide size distribution improve the filament by decreasing the overall viscosity of the binder and powder mixture during compounding. It is important to have a maximum load of solid ceramics to minimize problems during the post processing [77].

Onagoruwa et al. [77] have attempted the fabrication of ceramics and composites using the FDC process. The binder system used polypropylene (PP), which was mixed with functional ceramic particles and then extruded in filament form for FDC. The porous ceramic part can be controlled directly using FDM technology in which fused silica, mullite and titania powder green filaments were loaded. The green filament parts were similar to injection-molded parts, containing 45 vol% thermoplastic binder. The binder system was developed to load 55 vol% of ceramic powders, including fused silica, mullite, and titanium dioxide. The fused silicon oxide feedback contains around 53 vol% pure fused  $\text{SiO}_2$  and 3 vol %  $\text{MgO}$  with the developed thermoplastic binder system. The feedstock of mullite contained around 47.93 vol% pure mullite powder, 6.85 vol%  $\text{Al}_2\text{O}_3$  powder and 0.69 vol%  $\text{MgO}$  with the developed thermoplastic binder system. The feedstock of titanium dioxide contained around 51 vol%  $\text{TiO}_2$  powder and 4 vol%  $\text{MgO}$  with the developed thermoplastic binder system. The developed thermoplastic binder system contained around 44 vol% polypropylene, 13.9 vol% elastomer, 18.7 vol% plasticizer, 7.8 vol% tackifier and 15.6 vol% wax (Table 2). The developed binder system was applied to fabricate filaments of fused silica, mullite and titanium dioxide.

**Table 2**  
Binder constituent(s) and their characteristics in FDC [77]

Binder constituent(s)	Characteristics
Base polymer (polypropylene)	The backbone of filament and gives strength
Elastomer	Provides elasticity and flexibility
Plasticizer	Provides plasticity to filament for spooling
Tackifier	Enables tackiness and provides flexibility
Wax	Reduces viscosity

Their paper discussed feedstock development, fabrication of parts, and techniques to improve the quality of parts during the FDC process. To fabricate high quality ceramic parts required two stages, binder removal and sintering. Different rates of heat were applied at different temperature intervals to prevent internal and external cracking of the samples. The first stage involved removal of the liquid binder components by capillary action at low temperature ( $<200^\circ\text{C}$ ), followed by decomposition and evaporation of the remaining binders at a high temperature ( $>200^\circ\text{C}$ ). The second stage was the sintering process, which involved a temperature of  $1650^\circ\text{C}$  and a holding time of 3 h. The green ceramic parts were successfully sintered to produce parts with minimal flaws. The green ceramic parts' filaments were fabricated with appearance and features similar to those of the existing polymer parts and wax treatment using FDM Table 2.

Jafari et al. [84] also proposed an application of the FDC process by using ceramic filaments which were used for the direct fabrication of advanced functional ceramics such as  $\text{Si}_3\text{N}_4$  and PZT (Partial Stabilized Zirconia) for high stiffness. However, some limitations were found during the preparation and creation of these ceramics. The failures due to frequent buckling caused a disruption of the process during extrusion. Moreover, the back pressure met during the deposition limited the volume fraction of powder in the filament. However, they provided a successful solution to this buckling problem of the fabricated part by cooling the filaments between the liquefier and rollers.

Li et al. [85] utilized a ceramic slurry as the starting material, instead of plastic filament. However, the use of the ceramic slurry presented limitations, due to the minimum diameter of the extrusion nozzle. According to the Hagen-Poiseuille equation (Eq. (4)), a slight decrease in nozzle diameter will significantly decrease the

flow rate of the suspension and requires greater pressures to extrude this suspension. Blocking of the flow may be encountered, especially for very small nozzle diameters (<0.3 mm) and high viscosity feedstock (Low binder percentage <25%).

$$\Delta P = \frac{128\mu LQ}{\pi d^4} \quad (4)$$

where  $\Delta P$  is the pressure loss,  $\mu$  is dynamic viscosity,  $L$  is the length of extruder,  $Q$  is the volumetric flow rate and  $d$  is the nozzle diameter.

Giberti et al. [11] presented a revolutionary additive manufacturing (AM) system and designed the nozzle and extrusion head in order to be able to extrude high viscosity suspension with low thermoplastic binder content (polyethylene glycol). The proposed system was a mixture of deposited work materials, extrusion system (head and nozzle) and deposition on a 5-axes work table, with a parallel kinematics 3D machine. The system allowed feeding through pellets (Mixture of yttria stabilized zirconia powders with lower fraction of thermoplastic binder) rather than filament for FDC. The heavy weight extrusion unit was fixed in space and the resulting extruded filament was deposited on a moving table with 5-axes, acquired with a parallel kinematics setting. As a result, a good surface quality of the deposited work could be obtained and the need for supports was reduced during deposition.

#### 2.4. Binder-based 3D printing technique

3D printing can jet the binder into the ceramic powder. This involves building a model in a build platform that is filled with ceramic powder. An inkjet printer head is used to apply liquid binder to the appropriate layer. When the binder is applied to the powder, the powder solidifies. The build platform is then lowered and another layer of powder is spread over the first, and the process is repeated until the part is complete within the powder bed [2]. The 3D component is supported by the surrounding unprocessed powder and it will be removed from the ceramic powder bed after it has been completely printed. The component is depowdered and then sintered, which causes the excessive binder to be evaporated, giving the component sufficient strength [2].

Withell et al. [2] used ceramic powder which was slowly built in layers to form a 3D component. According to them, this method provides sufficiently low-cost 3D printing for ceramic materials. Using the Z-Corporation (Z-Corp) printer, they explored the potential for a wide range of applications, thus suggesting the need for future study. The Z-Corp printer uses an HP10 cartridge as a printer head with an ink viscosity of 1.35 cps and a surface tension of 45 dynes/cm [2]. The main function of the printer is to cut the solid object into digital cross sections and create a 2D image for each 0.01016 cm slice along the z axis until the part is complete. Additionally, it also provides the functions such as viewing, orienting, scaling, coloring and labelling for 3D components.

The calcium phosphate ( $\text{Ca}_3(\text{PO}_4)_2$ ) bioceramics are a primary focus for synthetic bone grafts used in bone tissue engineering application. This is because they show excellent osteoconductive properties due to their chemical composition being naturally similar to human bones and providing sufficient mechanical strength. Binder-based 3D printing has been employed to fabricate porous scaffolds where the calcium phosphate powder is temporarily bound by an adhesive polymer and then permanently bound by sintering of the printed green body [86]. Binder-based 3D printing was found to increase the surface accessibility of the scaffold structure for the liquid medium, through induced porosity. According to Criales et al. [63], hydroxyapatite scaffolds fabricated by 3D printing were highly appropriate for bone tissue applications. With a scaffold design with inclined layers of 45°, the

scaffold fabricated enables cell proliferation into the inside of the structure without clogging. With this designed structure, a modified cell-seeding protocol and seeding efficiency was improved. Khalyfa et al. [12] established a ceramic powder blend containing tetra-calcium phosphate as reactant with calcium sulfate or  $\beta$ -tricalcium phosphate as biodegradable fillers. The 3D printing equipment can be used to print that material with an aqueous citric acid solution as binder. No organic solvents are needed in the printing process. The ceramic blend can be used for human bone repair in load-bearing application fields. Their study also demonstrated that objects with complex internal architecture and shape can be produced using the described powder-binder system [87].

Wu et al. [14], explored a new method to prepare hierarchical scaffolds with controllable pore architecture, excellent mechanical strength, and mineralization ability for bone regeneration application by a modified 3D printing technique using polyvinylalcohol (PVA) as a binder. This method provides a new way to solve the commonly existing problems of inorganic scaffold materials: for example, uncontrollable pore architecture, low strength, high brittleness and the requirement for the second sintering at high temperature. According to their findings, the obtained 3D printed scaffolds can achieve a high mechanical strength which is about 200 times than that of the traditional polyurethane foam fabrication method. They developed 3D printed scaffolds with excellent for bone regeneration, highly controllable pore architecture, excellent apatite-mineralization ability and sustained drug-delivery properties.

As seen in this section, the researchers use different binders to solidify the powders and also to fabricating customized bone scaffolds that reflect the exact dimension of human bone defects. This binder has been characterized on the basis of 3D printing by their many advantages such as diffusion of powders and binders, depowdering, sintering, post-processing treatments, mechanical strength and feature customization [73]. A summary of these features is presented in Table 3.

### 3. Raw ceramic materials used in 3D printing

3D printing uses the potential of ceramic powder deposition to produce porous ceramic parts. In many cases, the ceramics are supplied as powders. A wide range of ceramics has been used in 3D printing, as illustrated in Table 4. Their material characteristics are the critical concern in this preparation for 3D printing. Selection of raw material is important as it will affect the part's functionality, mechanical properties and its structural properties. The selection of raw materials depends on the machine's limitations and the specific requirements of the final produced parts. Some deposition of these ceramic materials requires the modification of industrial 3D printer machines. The materials are normally loaded into the 3D printer and the parts with predefined shape, pore and strut size are printed [23]. In particular, they provide a sufficiently low cost solution for a wide range of applications [2].

In tissue engineering, the selection of materials must incorporate the consideration of mechanical properties and bonding strength, especially at the scaffold-bone interface. The advantages of this 3D printing is to make scaffolds with required pore shape and size, surface morphology and scaffold shape [108–111]. Bioactive inorganic materials, such as hydroxyapatite,  $\beta$ -tricalcium phosphate ( $\beta$ -TCP) and bioactive glass have been designed as 3D porous scaffolds for bone regeneration, due to their excellent osteoconductivity [14,87,112]. However, their inherent brittleness and low mechanical strength are the main disadvantages for developing 3D scaffolds, thus limiting their further application in the medical field [14,113–115]. Hydroxyapatite is a promising ceramic

**Table 3**

Binders used in 3D printing for ceramic materials.

Ceramic Powder	Binder type	Layer thickness	Post-processing	References
HA	- $\alpha$ -n-butyl cyanoacrylate (NBCA) - Polyvinyl Alcohol (PVA)	0.15–2 $\mu\text{m}$	- Vacuum oven dried 72 h at 70 °C	[88–90]
50 wt%HA 50 wt%PVOH	Water based binder	100 $\mu\text{m}$	Vacuum oven dried for 6 h at 60 °C - Sintering program: (1) Between 30–230 °C with 0.5 °C/min, (2) Between 230–1300 °C with 2 °C/min. (3) Time held 1 h at 1300 °C (4) Cooled to 30 °C with 2 °C/min	[91]
25 wt%HA 75 wt% CaSO <sub>4</sub>	Water based binder (ZB7, Z Corporation, UK)	-	- Oven dried 1 h at 70 °C	[92]
HA/ $\alpha$ -TCP	- phosphoric acid (8.75 wt%) + Non-cytotoxic surfactant (0.25 wt%) + Collagen 1–2 wt%	89 $\mu\text{m}$	- Phosphoric acid (0.1 wt%) flash dipping - Deionized water washing for (6 min) - Neutralized collagen gel Coating (0.5 wt%)	[86]
35 wt%HA 35 wt% $\beta$ -TCP 30 wt% modified acid-hydrolytic dextrin	15 wt% Water-glycerol	100 $\mu\text{m}$	- Oven dried 2 h at 75 °C - Oven dried 120 °C with 5.5 °C/min - Time held 1 h at 350 °C - Sintered at 1200 °C for 4 h - Grinded with 80 $\mu\text{m}$ grit SiC sandpaper - electrically Sintering at 1250 °C for 2 h (Air conditions)	[93]
-HA/TCP	10–14 wt% Schelofix (water based binder)	200 $\mu\text{m}$ ; 250 $\mu\text{m}$ ; 300 $\mu\text{m}$	- 10 wt% phosphoric acid hardening: (partial dipping)	[17,94]
$\alpha$ -TCP	10 wt% phosphoric acid	50 $\mu\text{m}$	- 10 wt% phosphoric acid hardening: (partial dipping)	[95]
- $\beta$ -TCP - SiO <sub>2</sub> -Mg doped $\beta$ -TCP	Solvent based binder	20 $\mu\text{m}$	- Oven dried 90 min at 175 °C - Conventional muffle furnace sintering at 1250 °C (2 h) - Microwave furnace sintering at 1250 °C (1 h) - Muffle furnace sintering at 1250 °C (2 h)	[96,97]
$\beta$ -TCP doping with SiO <sub>2</sub> -ZnO	Water based binder	-30 $\mu\text{m}$	- Autoclaving at 121 °C (20 min)	[98]
$\beta$ -TCP	20 wt% phosphoric acid	-	- 20 wt% phosphoric acid stored (3 min) - Monetite dehydration and autoclaving sterilization (121 °C; humidity 100%; 30 min)	[99,100]
$\beta$ -TCP	Aqueous based binder	20 $\mu\text{m}$	- Oven dried 90 min at 175 °C - Conventional muffle furnace sintering at 1150 °C (1–2 h) - Conventional muffle furnace sintering at 1250 °C (1–2 h)	[101]
- 45 wt% $\alpha$ -TCP - 55 wt% $\beta$ -TCP	20 wt% Phosphoric acid	-	20 wt% phosphoric acid hardening (full dipping)	[102]
TCP	20 wt% Phosphoric acid	125 $\mu\text{m}$	- Autoclaving at 134 °C (2 h) - Binder solution hardening (30 sec)	[103,104]
TCP +CaCO <sub>3</sub>	10 wt% phosphoric acid	112 $\mu\text{m}$	- Drying in air - Sintered at 1200 °C for 10 h with (1 °C/min) - Dipped in phosphate buffered saline (6 days) - Followed by air drying and immersed in 2.5 ml of a 10 wt% of poly(D,L-lactid-co-glycolide)-acid/acetone solution.	[105]
Farringtonite modified + 20 wt% diammonium hydrogen phosphate (DAHP)	0.75 M diammonium hydrogen phosphate + 0.75 M ammonium dihydrogen phosphate	125 $\mu\text{m}$	- binder solution hardening (24 h) - Distilled water rinsed (3times) - 70 vol% ethanol Soaked - Drying in air	[106]
CaSO <sub>4</sub> based powder	2-Pyrrolidone(ZB63) (water based solution)	87.5 $\mu\text{m}$ , 100 $\mu\text{m}$ , 112.5 $\mu\text{m}$ , 125 $\mu\text{m}$	- Dried in a building box 1.5 h - Post hardened	[23]
Plaster- CaSO <sub>4</sub>	Epoxy ZMax resin (ZB-58)	-	Infiltrated overnight to dry	[107]

material because the chemical composition is comparable to the inorganic part of native bone. It can form an interconnected pore network with both micro- and macroarchitecture. Pore sizes with diameters above 300  $\mu\text{m}$  are recommended to promote good vascularization and attachment of bone cells to guide their growth into all three dimensions [87]. The use of 3D printing allows the production of scaffolds with defined and reproducible internal structures, directly from computer data.

The timing effect between absorption and tissue growth rate is crucial to choose the suitable material from a technical point of view. Hence, another group of researchers (Inzana et al.) used 3D printing of calcium phosphate scaffolds, which are promising candidates for making synthetic bone graft substitutes with improved performance [86]. This is because calcium phosphate has a chemical similarity with bone materials. Essentially, some calcium phosphates such as  $\beta$ -tricalcium phosphate ( $\beta$ -TCP or Ca<sub>3</sub>(PO<sub>4</sub>)<sub>2</sub>), are

known to deliver a smooth transition between a bone flaw and mature bone. Further studies by some researchers also proved that the addition of SiO<sub>2</sub> and ZnO dopants to TCP scaffolds increases cell viability in different pore size ranges [116,117].

Recently, silica bioceramics have been broadly used for bone rebuilding and bone tissue application, because they have good mechanical properties, bioactivity and biocompatibility [14,118,119]. SiO<sub>2</sub>-sol mixed with CaCO<sub>3</sub> powder has been extensively studied and used to fabricate the porous structure of green ceramic part [120]. The silicate materials bond quickly to both hard and soft tissues and improve bone regeneration [121]. Silica powder acts as a filler substance to form the network structure and increases the mechanical properties, whereas CaCO<sub>3</sub> powder serves as a solid content and filler substance after sintering. Moreover, it has been found that these silica biomaterial scaffolds can enhance the mechanical properties after sintering [120]. Shao et al. [13]

**Table 4**

Raw ceramic materials used in the 3D printing process.

Powder	Ingredients	Particle size	Bulk strength	References
SiO <sub>2</sub> + CaCO <sub>3</sub>	SiO <sub>2</sub> sol: SiO <sub>2</sub> powder (20:80) + CaCO <sub>3</sub> (0, 5, or 9 wt%)	25 µm	47 MPa compressive (CaCO <sub>3</sub> 5 wt%) at 1300 °C	[120]
Leucite- glass ceramic (Vita VM-13)	SiO <sub>2</sub> (59–63 wt%), Al <sub>2</sub> O <sub>3</sub> (13–16 wt %), K <sub>2</sub> O(9–11 wt%), Na <sub>2</sub> O(4–6 wt%)	~18 µm	~120 MPaFlexural	[122]
Alumina (RC172-DBM)	Undoped MgO doped	75–150 µm 10–25 µm	231 MPa Flexural (Undoped) 324 MPa Flexural (MgO doped)	[123]
Hydroxyapatite (HA SP19)	polymeric additives	63–80 µm	13.7 MPa compressive	[87,124]
β –tricalcium phosphate	CaCO <sub>3</sub> + CaHPO <sub>4</sub>	10–25 µm	2.3–8.7 MPa compressive	[112,125,126]
Zirconia	27 vol% 3 mol%YSZ + 55 vol% H <sub>2</sub> O + boehmite sol and dispersants	90 nm	763 MPa Flexural	[36]
Bioactive glass ceramic α/β- tricalcium phosphate	Si:Ca:P molar ratio (80:15:5) Undoped Doped (0.5 wt% SiO <sub>2</sub> + 0.25 wt% ZnO)	<45 µm 550 nm	16.10 ± 1.53 MPa compressive 1.73–5.52 MPa compressive(Undoped) 4.31–10.32 MPa compressive (doped)	[14] [117]
Mg-doped wollastonite + β- tricalcium phosphate	CaSiO <sub>3</sub> –Mg (2.12 wt% Mg) + β-TCP (0–30 wt%)	<2 µm	80–100 MPa compressive (CaSiO <sub>3</sub> –Mg + 20–30% β-TCP) 120–140 MPa compressive(CaSiO <sub>3</sub> –Mg + 10–20% β-TCP)	[13]

developed high strength magnesium-doped wollastonite (CaSiO<sub>3</sub>–Mg)-based scaffolds through 3D printing technology. Integration of β-TCP can be easily modified sintering properties of scaffolds CaSiO<sub>3</sub>–Mg. The scaffold structures with a high fraction between (20–30%) and low fraction between (10–20%) β-TCP showed high mechanical strength properties (80–100 MPa or 120–140 MPa) after experiencing single or double stage sintering. Single step sintering was performed at a target temperature (1120 °C, 1150 °C, or 1180 °C) for 3 h, while two step sintering involves three heating programs (1120 °C, 1150 °C, or 1180 °C) held for two time lengths (45 min or 15 min). The scaffold was then rapidly cooled down to 1060 °C within 10 min and held at this temperature for 3 h. The CaSiO<sub>3</sub>–Mg with TCP 10 and 20% (~320 µm pore size) had more than 100 MPa in compression strength with ~52% porosity. Particularly, the scaffolds preserved significant strength (more than 50 MPa) after dipping in liquid buffer for a long time period (6 weeks). Their conclusions established that CaSiO<sub>3</sub>–Mg/TCP based scaffolds are promising for treatment of some human bones with defects, especially for the repair of load-bearing bone. The CaSiO<sub>3</sub>–Mg ceramic, which making the porous scaffolds, used well to enhance the wide area of segmental bone defect regeneration and repair in situ.

Different ceramic materials require parameter optimization for the process in order to fabricate a quality porous part. In bone tissue engineering, for example, the ceramic must have excellent bioactivity, osteoconductivity and similarities in composition to bone [116]. The control of fine features, including interconnected porosity, must be taken into account. Moreover, the structural designs and post-processing conditions can influence the mechanical strength of 3D printed scaffolds [15]. Tarafder et al. [101] reported the fabrication of 3D interconnected macroporous TCP scaffolds with controlled internal architecture by direct 3D printing. TCP scaffolds (27%, 35% and 41% macroporosity with different pore sizes of 500 µm, 750 µm and 1000 µm) were respectively fabricated by a direct 3D printing technique. The research showed that there was good cell adherence and cell ingrowth into the pores of scaffolds. Thus, TCP scaffolds have great potential in tissue engineering applications for bone tissue repair and regeneration.

#### 4. Depowdering process

Depowdering is a post-processing stage to remove the unbounded grains from the pore structure. After 3D printing, the

green ceramic body is removed from the build platform, and the loosely adhering powder is removed by dry ultrasonication or air blowing [19,101]. Depowdering is critical in binder-based 3D printing processes for green ceramic structure stability and architectures with complex interconnected porosity. To control the porosity and pore size in the center of a large scaffold continues to pose a challenge. The removal of loose powder from the printed body can easily crack a green part, due to its low green density at this stage [116]. Moreover, if certain internal channels are filled or blocked through unbound powder during an incomplete depowdering step in the process, the porosity of the part will be decreased.

Depending on the CAD model design and the 3D printing method, the support material may be needed for the fabrication, and thus removal of these support materials must be appropriate. The interior details must be fully disclosed to achieve the 3D printed actual features. The removal of the loose powder from outer surface is comparatively easy through blowing air. If the powder particles are loose in the inner parts, then additional wet methods, such as ultrasonication or microwave assisted boiling of the sample may be required. However, these methods can only be achieved if they do not dissolve the binder, to avoid mechanical disintegration of the printed sample [127].

The effect of printing orientation (parallel to the directions of X, Y and Z) and layer thickness on the depowdering process is also a concern. Farzali et al. [23], fabricated the structure of scaffolds with different pore sizes of 0.4, 0.6 and 0.8 mm. Depowdering of the ceramic samples with 0.4 and 0.6 mm pore sizes could not be implemented properly, and those ceramic samples were found to have deteriorated scaffold structures after 3D printing. To provide pore size 0.8 mm printed with a different layer thickness and printing orientations, more properties were considered. The 3D samples printed in the direction X were found to be somewhat more depowdered if compared with those printed in the direction Y. A longer average time was needed to completely depowder the ceramic printed samples in the direction Z. Asadi-Eydivand et al. [128] discovered that insufficient compressive strength of the Z-direction preparation led to the fracture of ceramic samples during this process. Fig. 12 shows the effect of different parameters on the compressive strength. According to the figure, the compressive strength of the 3D printed porous ceramics in the X direction was significantly higher than that of the Z direction fabrication. Insufficient compressive strengths of the Z direction fabrication led to the fracture of ceramic samples during depowdering.

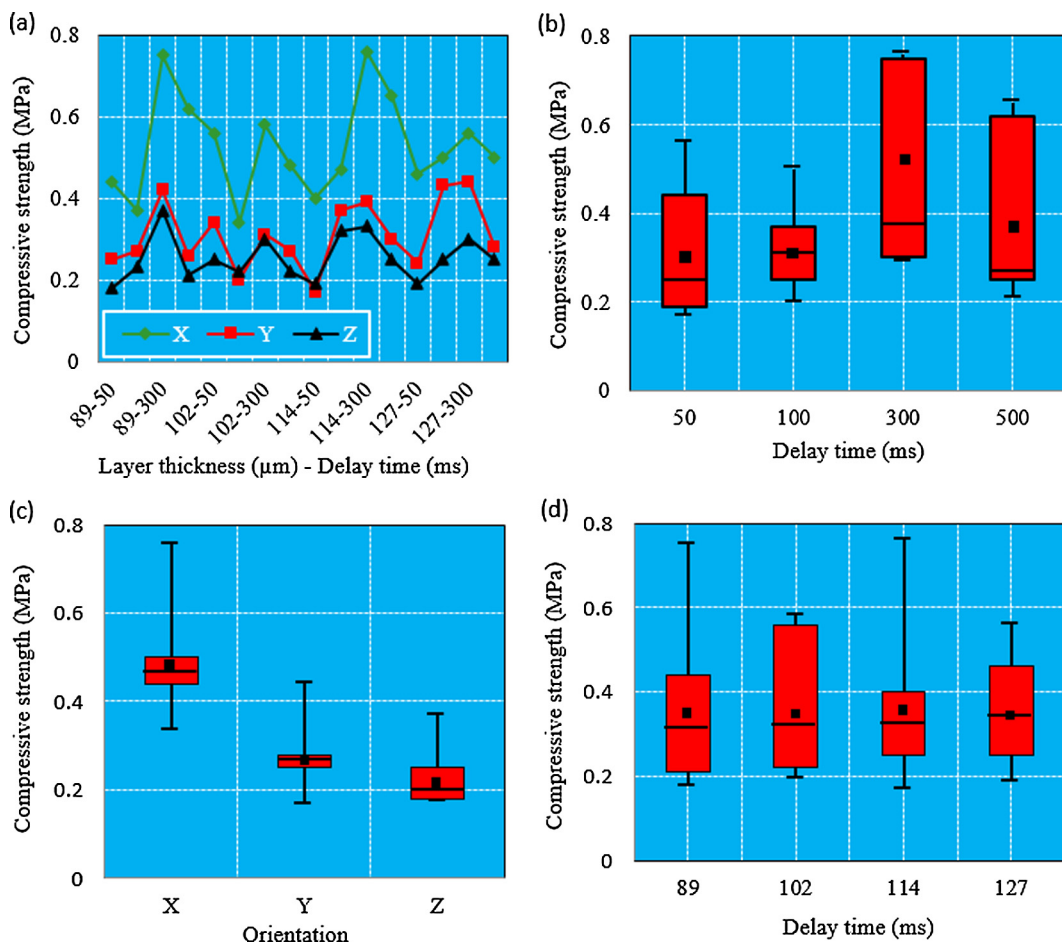


**Fig. 12.** The effects of 3D printing parameters on the compressive strength with (a) layer thickness-delay time for X, Y, and Z build orientations, (b) delay time, (c) orientation and (d) layer thickness [128].

Furthermore, the samples printed with a 300 ms delay time between spreading each layer had more compressive strength. For the materials with low compressive strength, it will be more difficult to remove the powder from the initial printed surface and a longer time will be necessary for the preparation of ceramic samples.

## 5. Characterization of ceramic powders

Ceramic materials have remarkable physical and chemical properties that make them applicable in an extensive range of fields. Fabrication by 3D printing of ceramic products has become attractive due to the adaptations and developments of the 3D printing methods [129]. Most of the researchers have used 3D printing as a tool to make scaffolds for tissue application. However, there is a relative lack understanding of the relationship between the properties of ceramic powders and the outcome of 3D printing. These powder parameters, such as particle size, flowability, roughness and wettability, have a significant effect on the printing accuracy. The general requirements of the ceramic powders used for 3D printing include the possibility to obtain layers, powder types that guarantee the printing quality and a rapid setting reaction between the binder and powder.

Butscher et al. [112] investigated the fluidity and stability of the powder, the wetting ability of binder particles, and the reaction between powder and binder. They concluded that promising results for the printing outcome can be expected for the powder using  $\beta$ -tricalcium phosphate with average particle size between

the range of 20–35  $\mu\text{m}$ . The results also showed that, for better quality, the compaction rate should be in the range of 1.3–1.4, flowability in the range of 5–7 and surface roughness of the powder bed (10–25  $\mu\text{m}$ ). These promising results required characterizations which were important for good printing outcomes. Various characterizations will be discussed in this section.

### 5.1. Effect of particle size for 3D printing

The ceramic powder particle size distribution is critical for enabling a well-packed, smooth powder bed for 3D printing. It is also important for dictating the intrinsic micro-porosity and resolution of the printed ceramic material [86,112]. Thus, the ceramic powder is sieved to remove particulate that is too large for accurate printing and too small to avoid agglomeration (Fig. 13). Larger particles have lower surface area per volume and are simpler for spreading. They have larger pores, which results in fabrication of more homogenous parts, as binders can penetrate into the powder bed efficiently. According to Yang et al. [122], irregular morphology and large particle size range may significantly reduce the powder's flowability during the 3D printing process. A press-rolling technique proposed by Yoo et al. [123], makes the layers of fine powder spread uniformly by rotating the spreader rod over the loosely packed layer to pack the powder rather than shearing away the excess powder.

Sometimes, finer powders are required to achieve finer micro-scale features, better surface finishes, thinner layers and to promote printability. However, fine powders encounter several

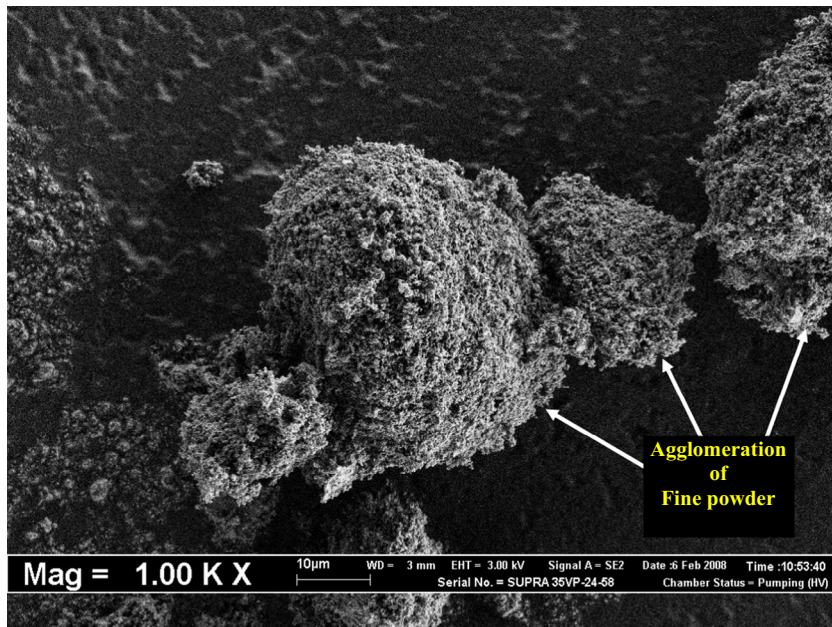


**Fig. 13.** The agglomeration effect of the fine ceramic powder for accurate 3D printing.

challenges in their direct application in the 3D printing process. Fine powders may exhibit a significant aggregation, which causes their inability to be spread uniformly in the printing process. There is a relationship between the powder's properties and its printability in a 3D printer. High specific surface area is beneficial because of the higher reactivity with the binder solution [112].

Small particles tend to agglomerate, because there is an attractive interaction between ceramic particles, which is principally determined by van der Waals forces. In very fine ceramic particles, these van der Waals forces can even dominate gravitational forces and cause significantly decrease in the flowability. Moreover, the irregular shapes of single and aggregated ceramic particles also induce poor flowability of particles during the 3D printing process.

The possibility to obtain a smooth powder layer depends on powder particle size. In a recent review by Vorndran et al. [130], it was found that the smaller-sized particles of ceramic powders, with dimensions smaller than 5  $\mu\text{m}$ , are prone to agglomerate due to the van der Waals forces, thus forming defects and craters on the surface of the powder during layer preparation. If it is necessary to use particles with dimensions smaller than 5  $\mu\text{m}$ , then it is recommended that the particles are granulated before use or preparation of suspensions. These smallest particles were useful for medical applications to elicit superior biological properties. A future challenge would be minimization of the size of the particles to ensure printability through a nozzle. Another challenge is related to the 3D printers, which are commonly designed for engineering applications. These parameters would need to be optimized in conjunction with the development of the technique, in order to create medical products of sustainable quality.

Particle size distribution influences the powder's flowability. Fine particles ( $<5 \mu\text{m}$ ) tend to form clusters and prevent uniform recoating during 3D printing techniques such as SLM. Large particles ( $>90 \mu\text{m}$ ) reduce the maximum layer packing density available. A mix of small and large particles is suitable for higher density because the small particles fill the void between the larger particles. For porous application, the use of a large fraction of particles is concerned. German [131] showed that if the amount of fine particles reaches 30%, a bi-modal mixture of powders with a size ratio of 1:7 can increase the powder density by 30%. If the amount

of fine particles ( $\leq 5 \mu\text{m}$ ) is too high, the agglomeration of the particles can eliminate their positive effects of filling up voids.

According to the concept of bimodal powder packing investigated by [131], the powder exhibits bimodal packing when small and large particles are mixed, thus improve the packing density of a powder. The smaller particles will fill in the cavities between the large ceramic particles. The small quantities of smaller powder will improve the density of the ceramic part. The optimal composition corresponding to the highest achievable density is illustrated in Fig. 14. In this figure, the density is calculated based on the weight fraction of large particles  $X_L^*$ . The best density is calculated from the amount of void space between large particles, which equals  $1 - f_L$ , where  $f_L$  is the fractional packing density of the large particles.

$$X_L^* = \frac{f_L}{f^*} \quad (5)$$

The best composition of fractional packing density  $f^*$  given as,

$$f^* = f_L + f_S(1 - f_L) \quad (6)$$

where  $f_L$  is the fractional packing density of large particle,  $f_S$  is the small particle's fractional packing density,  $f^*$  is the fractional packing density of the best composition, and  $X_L^*$  is the weight fraction of maximum packing density for large particles. All represent the dimensionless [0,1].

## 5.2. The effect of flowability for 3D printing

Flowability of ceramic powder is an important parameter for 3D printing technology. It is critical in this fabrication process, as it determines its ability to be spread. It can be determined by particle size, size distribution, surface roughness, and shape [116]. High flowability of powders allows sufficient rolling for the construction of a thin layer (recoating) and the issuance of high-resolution 3D printing. A very low flowability decreases printing resolution, because of insufficient recoating. However, very high flowability does not provide the stability and abundance of powder in the bed for 3D printing [112]. Fine powders do not generally flow well enough to spread into defect-free layers. Their high surface area

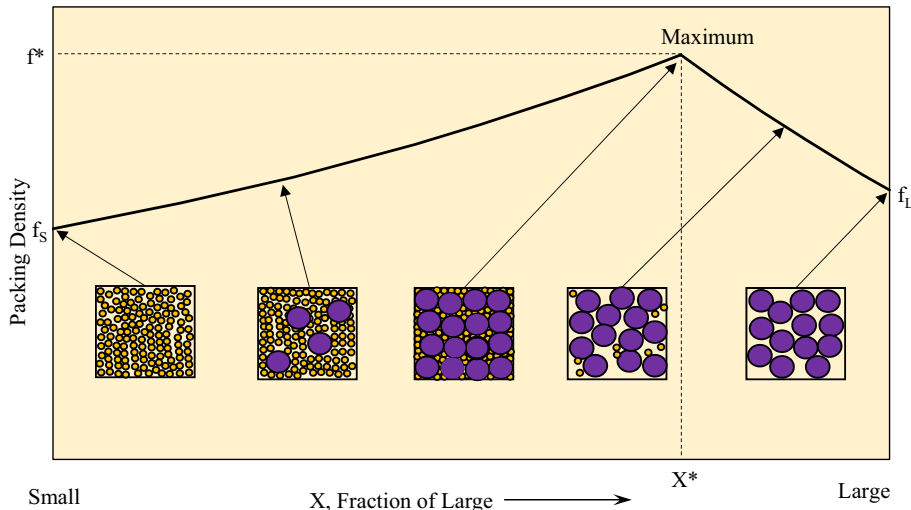


**Fig. 14.** Bimodal powder packing (variation of the packing density with particle size, volumetric porosity and powder particulate size for 3D printing process) [131].

causes increased cohesive strength of the unpacked powder and decreased flowability [123]. A modification can be made to the conventional spreading method to improve the flowability of fine powder. A press-rolling technique is the initial low packing of the fine agglomerate of powders. The load was applied to the powder bed by stream rolling the spreader rod in order to spread uniform thin layers of fine powder. Uniformity in the microstructure of green samples was necessary to ensure the elimination of defects upon sintering.

The flowability can be measured by either the ring shear test method or custom-made glass funnel method. In the ring shear tester, the cell was filled with a volume of 30 ml powder, the pre-shear stress was set to 1500 Pa. Then subsequently shear stresses of 300, 750 and 1200 N was applied. The flowability was expressed by flow factor  $ff_\beta$  [112]. The flow factor is defined as the ratio of the consolidation stress  $\sigma_1$  and the compression strength  $\sigma_2$ .

$$ff_\beta = \frac{\sigma_1}{\sigma_2} \quad (7)$$

The qualitative ranges are used to classify the flowability, which could be represented as:  $ff_\beta > 10$  for free flowing;  $4 < ff_\beta < 10$  for easy flowing;  $2 < ff_\beta < 4$  for cohesive;  $1 < ff_\beta < 2$  for very cohesive;  $ff_\beta < 1$  for non-flowing.

In the custom-made glass funnel technique, a glass funnel with a diameter of 46 mm and an angle of 35° with different orifices diameter (8, 12, 18, 24, 30 and 36 mm) was used to assess the flowability. The flowability depends on the pass or non-pass powder ranking for different cylinder orifices. According to Chumnan-klang et al. [132], they used the Hall flow meter technique to measure the flow rate of raw hydroxyapatite powders and spray-dried powders. A weighed amount of oven-dried powder was placed so as to pass through the small opening of a glass funnel and the total time required was recorded by a timer. The measurement can be calculated from the following equation:

$$\text{Flow rate (g/s)} = \frac{\text{Mass weight (g)}}{\text{Time (s)}} \quad (8)$$

### 5.3. The effect of wettability on 3D printing

The wettability of the ceramic particles to the binder solution is another critical factor for 3D printing. The binder saturation depends on the powder wettability, in terms of the amount of

binder solution absorbed by the ceramic powders. The volume of binder distributed within the ceramic powders determines the mechanical strength properties and the resolution (voxel size) of the final bulk [133]. However, the wetting mechanism of a ceramic powder by polymer binder droplets is very difficult. A very low wettability of fine powder can result in rearrangement of the powder. Hence, this may lead to weak powder-binder integration and be detrimental to further 3D printing fabrication. A very high wettability and slow reaction with the powder will decrease the size of the smallest features and lead to extensive binder spreading [112,134]. Thus, the wettability of the powder, which is related to the particle chemistry and surface energy, determines the print resolution and tolerance achievable [135].

The contact angle between the interface of liquid/gas or liquid-solid can be used to measure the wettability of the powder. The capillary penetration method often gives robust result for wettability. A schematic diagram of this method can be found in Fig. 15. In this method, the compressed powder was filled in a glass-cylinder with a permeable bottom. The capillary force was determined mostly by the space between particles in the different characteristics and the surface dimensions. The measurements for wettability were implemented using a Tensiometer K100 (Krüss, Germany). The contact angle,  $\theta$  can be derived from Washburn's equation:

$$\frac{m^2}{t} = c \times \rho_L^2 \times \sigma_L \times \cos \theta \times \eta_L \quad (9)$$

where  $m$  is the mass of absorbed fluid,  $t$  is the absorption time,  $c$  is the capability constant,  $\rho_L$  is the liquid density,  $\sigma_L$  is the surface tension of the fluid and  $\eta_L$  is the dynamic viscosity of the fluid. The penetration rate ( $m^2/t$ ) is determined by linear regression in the linear part after initial wetting and before the liquid reaches the top of the wetted powder specimen. The capability constant,  $c$  is determined by using a wetting liquid. Ideally, the contact angle measurements should be performed with the fluid used for 3D printer.

## 6. Characterization of porous ceramic parts

### 6.1. The effect of porosity after preparation in the 3D printing process

Porosity is a structural property of the ceramic materials in 3D printing technology. It is known to be another factor and a measurement of the capacity of ceramic materials to store fluids inside a structure. A porous ceramic medium is most often characterized

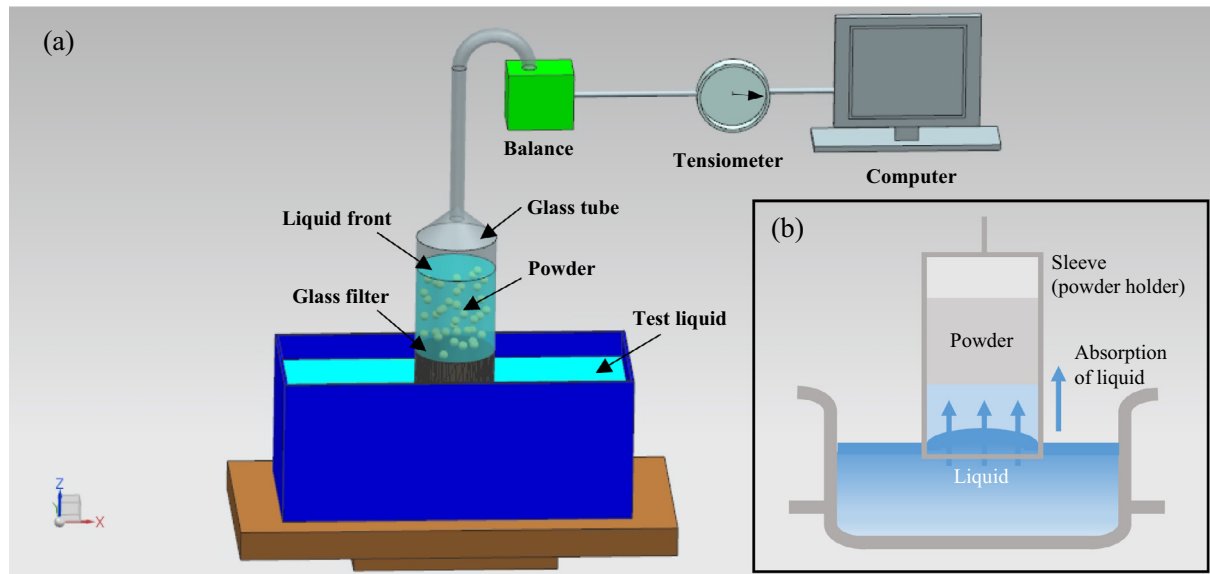


**Fig. 15.** (a) Schematic diagram of the contact angle measurement by the Washburn method, (b) Explanation of the Washburn method [112].

by its porosity, which can influence its most important properties, which include the fraction of the volume of voids over the total volume of the ceramic material. Asadi et al. [128] studied the effect of each setting parameter on the porosity of 3D printed ceramics. According to this study, the samples printed in the X direction with 114 µm layer thickness and 100 ms delay the time between spreading each layer; moreover, the ceramic samples printed in the Z direction with 102 µm layer thickness and 500 ms delay, had the most open porosity (Fig. 16). Thus, the 3D printing of a porous structure becomes more important in bone scaffold fabrication and other applications.

Bone is capable of self-regeneration; however, this regeneration is limited to a few millimeters distance from healthy bone. Therefore, in order to improve bone regeneration, bone defects must be filled with a porous structure to allow ingrowth of bone and blood vessels, at the same time restricting soft tissue ingrowth. Generally, it is agreed that the porous network should involve interconnected pores with a range of diameter between 50 and 1000 µm [136]. Pore network and the size of the 3D printed scaffold can be observed by optical microscopy and scanning electron microscopy. The porosity also can be measured by a liquid displacement method. In this method, the scaffold's structures were dipped in a graduated cylinder with a recorded volume of ethanol,  $V_\alpha$ . Then, the cylinder was put in vacuum that forced the ethanol liquid into the inside pores of the scaffold until no more bubbles were seen, the volume was marked as  $V_\beta$ . The scaffold structure was removed and the volume of the remaining ethanol was recorded as  $V_\gamma$ . The porosity  $P$  was calculated by the following equation:

$$P = \frac{(V_\alpha - V_\gamma)}{(V_\beta - V_\gamma)} \times 100\% \quad (10)$$

Sometimes because of the paste's viscoelasticity, the scaffold strands, once dispersed, will deform and fuse together. As the result, the actual size of the pores and scaffold's porosity are reduced from those designed. The pore sizes in the vertical direction could reduce by up to 50% compared to the design values. As size of pores and porosity can affect the mechanical strength properties of the fabricated parts, this may significantly degrade the performance of the scaffold structure as applied in tissue applications.

Beside the effect of pore size and porosity on the scaffold's mechanical properties, these factors also influence its biological properties. The porosity increases the rate of both tissue growth and deposition of extracellular matrices and cells may not grow in scaffolds where the sizes of pores are very small [137]. The size of a pore can influence cell attachment and cell formation. Hence, down to a certain range, the porosity may result in poor mechanical strength properties of the scaffold. Therefore, a scaffold structure manufactured with the desired porosity and pore size is of paramount importance in tissue applications but still a challenge. Fig. 17 shows the schematic of the internal structure of tissue scaffolds made from 3D printing.  $l_z$  is the vertical pore size while  $l_{xy}$  is the horizontal pore size.  $L_x$  is the distance between two adjacent horizontal strand centers and  $D$  is the diameter of the strand. In the horizontal direction, the fabricated pore size is equal to the designed pore size. However, the pore size in the vertical direction will be considerably decreased because of the two contacting strands with each other.

The basic requirement for applications of scaffold tissue is that the structure must be porous enough to support bonding, which has been shown to be nearly 60 vol% porosity [79]. Bose et al. reported that the pore size sufficient for applications of human bone tissue is in the range 100–800 µm for cell attachment and vascularization [138]. The structure of a porous scaffold is required in bone tissue engineering to allow cell differentiation, proliferation, and tissue growth at the end of the process. The permeability of liquids through the structure of the bone scaffold is important to provide the deployment of food and disposal of waste from the renewal site. Maximum permeability is needed, as far as is possible without compromising the mechanical properties. There are different architectures for scaffold pores, which includes a basic circular shape, hexagon, cube, diamond, gyroid and salt-leached structure [62,79]. Tseng et al. [79], defined the scaffold porosity for both hexagonal and circular shapes through a regression model using Minitab 15 software. According to that research, the pores for 134 samples were produced from 0.5 mm to 1 mm with an increment of 0.1 mm. Five factors were considered in this regression analysis, including the size, distance, shape, surface area and number of pores. Each factor presents effects both independently and interactively. The regression model can be assumed as follows:

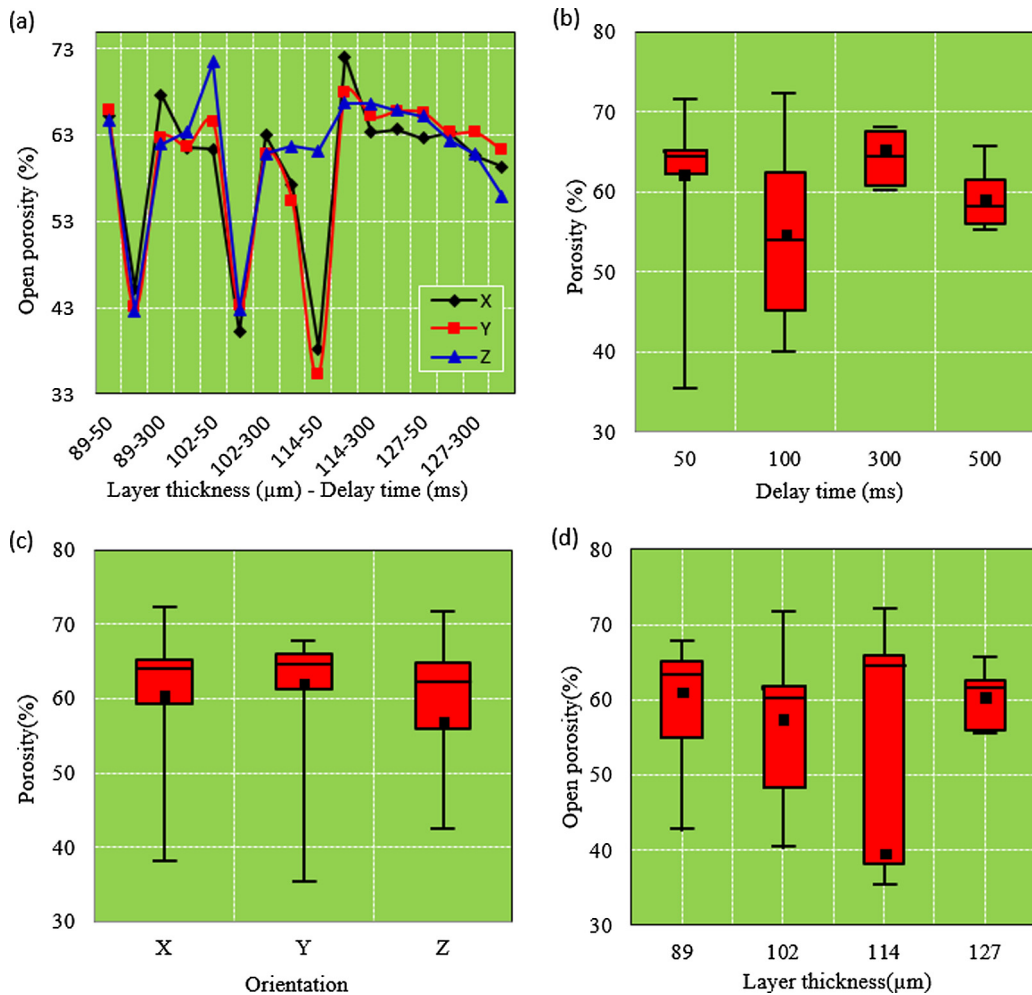


**Fig. 16.** The effects of 3D printing parameters on the open porosity with (a) layer thickness-delay time for X, Y, and Z build orientations, (b) delay time, (c) orientation and (d) layer thickness [128].

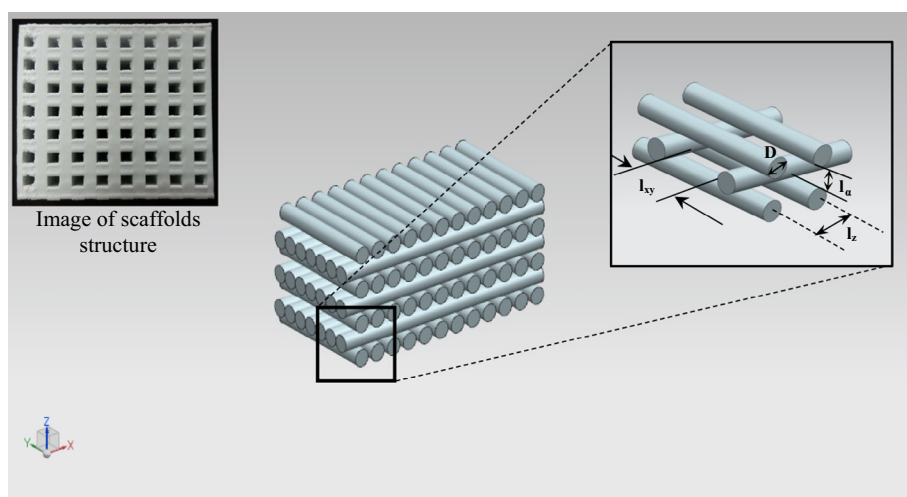


**Fig. 17.** Schematic diagram of the tissue scaffold's internal structure made from 3D printing [137].

$$\begin{aligned}
 Y &= 0.53 + 0.15 * R + 0.03 * D_b + 0.08 * P_N + 0.04 * S - 0.02 \\
 &\quad * S_A - 0.04 * R * P_N + 0.02 * R * S - 0.02 * D_b * S - 0.05 \\
 &\quad * D_b * S_A + 0.03 * P_N * S + 0.02 * S * S_A
 \end{aligned} \tag{11}$$

where  $Y$  is the porosity,  $R$  is the pore radius,  $D_b$  is the distance between pores,  $P_N$  is the number of pores,  $S$  is the shape (hexagonal or circular) and  $S_A$  is the surface area. The adjusted R-square value was 90.25%, which was shown correctly for this regression model

to predict the porosity. It was confirmed that all five factors can be used in the design with significance between the actual and predicted porosity values (Fig. 18). According to this model, maximum porosity can be achieved when shape number, radius, the distance between pores and the number of pores is high. Their outcomes also indicated that a hexagonal shape is better than a circular pore shape, due to further edges, and is more suitable for the cultivation of cells [79].

There are open, interconnected and closed pores in a porous scaffold. The open and interconnected pores contribute to cell ingrowth and permeability, while the closed pores only decrease strength. Thus, it is optimal to maximize the open pores and minimize the closed pores in a condition where the mechanical strength properties are not compromised [128]. Wu et al. [139], believe that the interconnective pores and controllable pore size of the fabricated scaffolds will benefit cell nutrient delivery and ingrowths. They found that 3D printing scaffolds improved stability and reproducibility to induce *in vivo* bone fabrication, if compared to those prepared by porogen methods. 3D printed calcium silicate scaffolds were found to improve the bone defect-healing ability more than  $\beta$ -TCP scaffolds fabricated by same method. Their results also suggested that calcium silicates scaffolds provide potential excellent bone regeneration material compared with  $\beta$ -TCP scaffolds.

## 6.2. Mechanical properties of 3D porous ceramic parts

The conventional fabrication of porous ceramics, such as salt-leaching, gas foaming and phase separation restrict the choice of materials and limit the freedom of design [140]. However, advances in 3D printing technology have significantly improved the control over whole design of solid and porous structures [141,142]. However, their low mechanical properties provide the main challenge in porous structure scaffolds and limit their application, especially when related to heavy load bearing. The mechanical properties of porous ceramics are influenced by the material, pore architecture and processing parameters (printing orientation, thickness of layer and delay time between spreading each powder layer) [62,128]. Thus optimization, compositional modifications and post-processing approaches can improve the mechanical properties of porous ceramics [140,143,144].

Tarafder et al. [101], studied the post-processing approaches for microwave sintering of 3D printing samples at 1250 °C for 1 h to improve the strength of the scaffold by decreasing the pore size. In their study, a maximum strength of  $10.95 \pm 1.28$  MPa was

observed for scaffolds with 500  $\mu\text{m}$  designed pores ( $\sim 400 \mu\text{m}$  after microwave sintering), which had 42% total open porosity. Their results showed that bioresorbable 3D-printed TCP scaffolds have great potential in tissue engineering for bone tissue repair and regeneration. In another study by Khalyfa et al. [12], they discovered that a mixture of tetracalcium phosphate (TTCP)/ $\beta$ -TCP could increase the strength of the 3D printed scaffold after sintering at 1400 °C. However, sintering a TTCP/calcium sulfate dehydrate composite caused a decrease in the strength, due to water release. The liberation of water results in an increase in the porosity, connected with an extensive weight loss and shrinkage of the samples.

Meanwhile, bioactive liquid phase sintering aids have also been reported to increase the strength of porous ceramics, according to Suwanprateeb et al.'s research [145]. They used the glassy phase added to 3D printed hydroxyapatite/apatite-wollastonite glass as a liquid phase sintering aid, and their results showed an increase in the strength of ceramic scaffolds from 1.27 MPa to 76.82 MPa when sintered at 1300 °C for 3 h. Khalyfa et al. [12] used another approach to increase the strength of ceramic scaffolds without impairing their biological properties by using monomer or polymer infiltration. In this approach, a mixture of bismethacrylated oligo-lactide macromer (DLM-1) containing 10 wt% of 2-hydroxyethyl methacrylate to increase the scaffolds strength before and after sintering. The immersion of hydroxyapatite scaffolds in triethylene glycol dimethacrylate (TEGDMA), 2,2-bis [4(2-hydroxy-3-thacryloyloxypropoxy)-henyl] propane (bis-GMA) resulted in an increase in flexural strength by at least 20 times [146]. Table 5 summarizes the mechanical strength properties of 3D printed structures of scaffolds for bone tissue engineering.

Shao et al. [13] showed the changes in the mechanical properties of bioceramic structure scaffolds when changing the TCP content from 0 to 30 wt% and sintering temperatures between 1120 and 1180 °C (Fig. 19). The amount of TCP can significantly influence the mechanical properties of the structure of 3D printed scaffolds. The compressive strength of the  $\text{CaSiO}_3$ –Mg/TCP scaffolds (1120 °C) reduced with increasing TCP content. When sintering at 1150 °C, the  $\text{CaSiO}_3$ –Mg/TCP<sub>x</sub> ( $x = 0, 10, 20$  and 30 wt%) showed higher strength between (~100 to 122 MPa), but their strength was reduced slightly with the increase in the content of TCP.  $\beta$ -TCP may adversely influence the bulk properties after sintering of  $\text{CaSiO}_3$ –Mg substrate. The researchers also considered that more  $\beta$ -TCP content and a higher temperature of sintering were needed to achieve a full densification and good mechanical properties. Instead, they found that the scaffold structure shrinkage was associated with temperature of the sintering and content of TCP, and

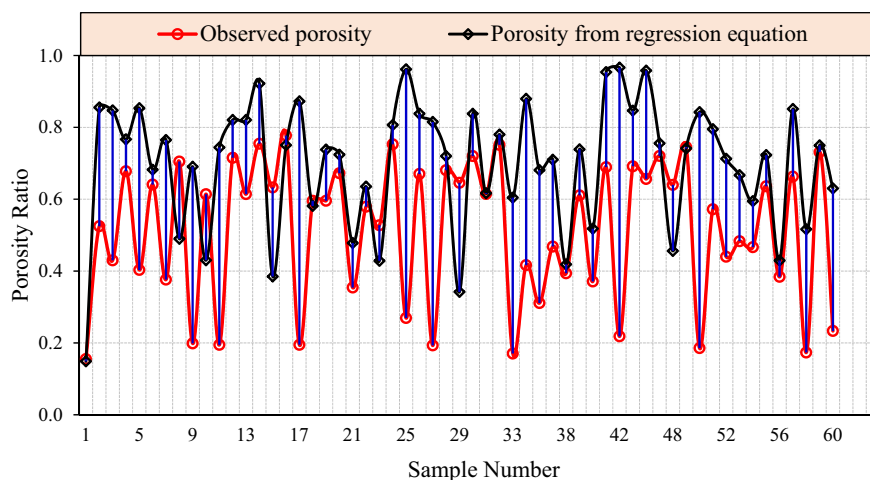
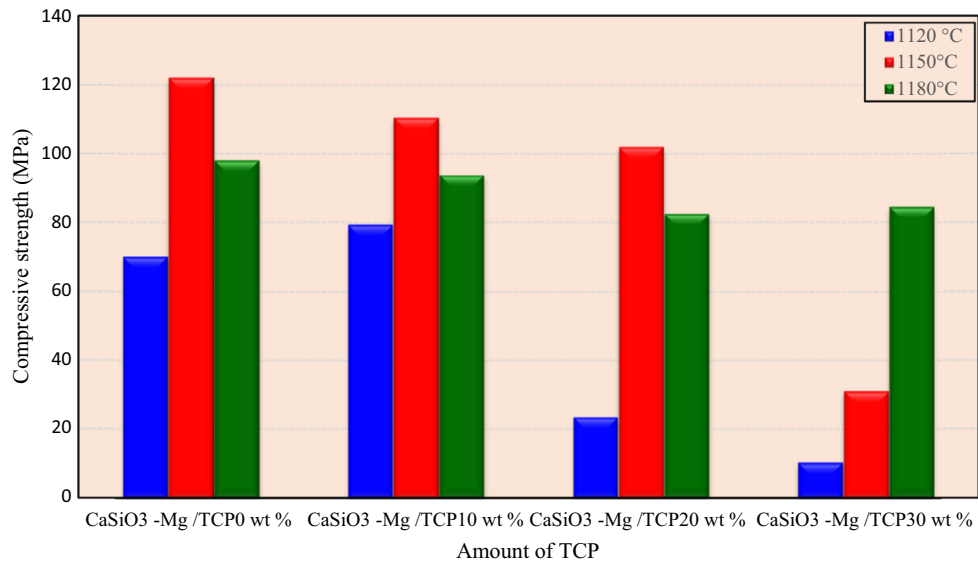
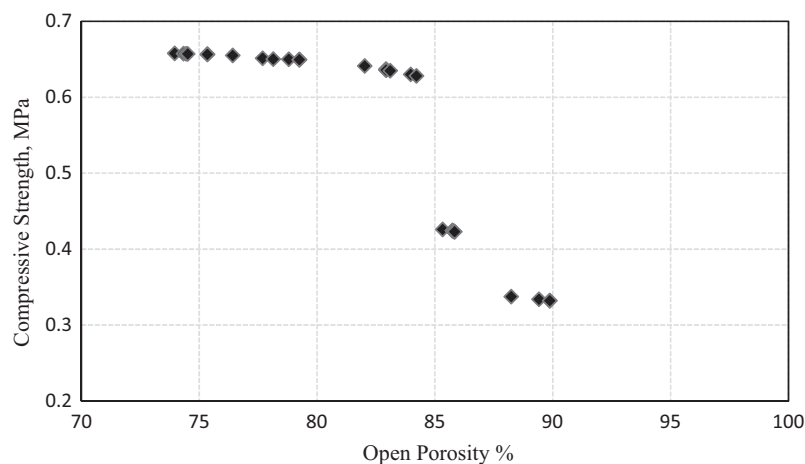


Fig. 18. Comparison between the actual and predicted porosity values [79].

**Table 5**

Mechanical properties of 3D printed scaffolds [116]

Material	Compressive strength/(Bending strength) MPa	References
TCP-sintered Conventionally at 1250 °C	6.4/(5.5)	[101,117]
TCP-sintered using microwave at 1250 °C	10.9	[101]
TTCP/β-TCP- without sintering	0.7	[12]
DLM infiltrated TTCP/β-TCP-without sintering	76.1	[12]
SiO <sub>2</sub> -ZnO doped TCP-sintered conventionally at 1250 °C	10.2	[117]
HA-without sintering	(0.69)	[146]
HA/A-W glass - without sintering	(1.27)	[145]
HA/A-W glass-sintering at 1300 °C	(76.82)	[145]
HA/bis-GMA- without sintering	(50)	[146]

**Fig. 19.** The relationship between the amount of TCP and compressive strength at sintering temperature 1120 °C, 1150 °C, and 1180 °C for 3hours respectively [13]**Fig. 20.** Compressive strength versus open porosity for porous ceramic [128].

thus related directly to their mechanical properties. The researchers found that most of the bioceramic porous materials revealed high shrinkage, around ( $\sim 28 \pm 1.5\%$ ), whereas, in comparison, the CaSiO<sub>3</sub>-Mg/TCP30 (1120 °C) showed only a lower shrinkage (11.5%). The significant pore shrinkage resulted in strong mechanical strength parallel to the orientation of the pores.

Since the pore-size parameter was beneficial to some applications, such as facilitating the bone ingrowth, nutrient delivery

and vascularization *in vivo*, a further evaluation relating the pore diameters to the mechanical properties is needed in future studies. Asadi Eydavand et al. [128] observed the relationship between the compression strength and porosity of porous ceramic structures. They found that the strength of the porous ceramic increases with decreasing pore size. Scaffold structures are highly porous 3D parts that are used to reproduce the natural extracellular matrix of human bone on the a short-term basis. Thus design and materials

for scaffolds are highly demanding from a technical point of view. Interconnected porosity together with optimal mechanical strength is a critical parameter that describes the performance of a scaffold structure.

This study [128] also used two optimization methods to obtain the best 3D printing parameter settings for small porous structures. Initially, a particle swarm optimization algorithm was used to obtain the best aggregated scheme of an artificial neural network (AANN). After that, they implemented the Pareto optimal front to determine the best 3D setting parameters for the scaffold's formation with the required porosity and compressive mechanical strength. They predicted the porosity and compressive strength of the 3D structure of scaffolds printed on a wide range of layer thickness, print orientations and time delays for the deployment of each layer. With this setting, they were able to predict the best mechanical properties and porosity, based on setting parameters. This approach also provides the information to design a porous ceramic structure and assess the impact of leading processing factors. Fig. 20 shows the decrease in mechanical strength due to the increase of open porosity.

In developing models for porous structures, Zein et al. [74] discussed the compressive properties which depend on porosity. They presented results for the variation of mechanical properties with porosity. Scaffold compressive stiffness  $E_s$  and yield strength  $\sigma$  decreased rapidly as the porosity increased. These declines were described using a power law function given by the Eqs. (12) and (13) respectively.

$$E_s = C_1(100 - P)^n \quad (12)$$

$$\sigma = C_2(100 - P)^n \quad (13)$$

where  $C_1$ ,  $C_2$  and  $n$  are constants whereas  $(100 - P)$  is the relative density.

The analysis of mechanical properties provided a better understanding of the nature of the anisotropic structure of different designs. Generally, it was found that the mechanical properties depend on the porosity and regardless of the size of the channel, this being in agreement with theoretical ideas on the properties and structural relationships of porous ceramics.

## 7. The future for 3D printing of porous ceramics

3D printing has been intensified in various areas of development in terms of resolution, materials and printing speed. The advance in 3D printing towards the use of ceramic materials has broadened its application, due to the energy efficient, fast, and flexible approaches that are made possible. It provides the possibility of fabricating green bodies at a high resolution and with complex shapes. Both external shape and internal characteristics such as pore size can be fabricated using Computer Assisted Design (CAD). For example, the use of customized 3D scaffolds with defined dimensions opens the possibility of tissue engineering of bones and other skeletal structures exactly tailored to the dimensions of the patient. 3D printing is a promising area to fabricate porous ceramic objects such as scaffolds structures due to its capability to fabricate complex 3D shapes with controlled internal structures. The porous ceramic models are readable by the 3D printer and can flexibly fabricate the model in a layer by layer fashion. Moreover, 3D printing can improve porous structure formation by controlling its microstructure and parameter optimization.

Basically, the parameters such as the flowability of powder and wettability need to be optimized to improve the quality of spreading ability, accuracy and tolerance achievable in the 3D printing output, particularly for bone tissue engineering. Powder flowability is the most crucial parameter in 3D printing technology as it

influences the ability of the powder to be spread. The factors that affect wettability and flowability, include particle size, surface area of the powders and the thickness of the 3D printed layer. From a medical point of view, the surface area of the powder influences cell attachment and proliferation, and the biodegradation kinetics of scaffolds. The desired thickness of a layer is partially determined by powder and geometry properties. Thinner layers can spread the polymer binder and excessive spread to other sites causes poor tolerance and resolution. However, thick layers require high concentration of ceramic particles to fuse with each other. Overall, for the best structure, particle size, pore size, thickness of layer and surface area are significant factors to obtain the most satisfactory results for a particular application.

In terms of the manufacturing aspect, 3D printing can provide benefits in producing porous ceramic parts. Evolution of 3D printing manufacturing involves prototyping and rapid tooling. Architects, artists and product designers can benefit from 3D printing technology to make prototypes for new ceramic structured designs. Most 3D printing still revolves around manufacturing considerations, in terms of easy production, low cost and ease of duplicating products. 3D printing allows for larger production runs, moreover different sizes and styles of the parts required can be easily produced. In the future, 3D printing in porous ceramic manufacturing technology can be used in a number of applications. For example, it is used extensively for catalysis, biomedical applications, filtration technologies and replacement automotive parts manufacturing. It can also be used to produce porous ceramic membranes, heat exchangers and energy storage, due to the competitive thermal properties and relative strength of the ceramic materials.

## Acknowledgement

The authors would like to thanks the Ministry of Education Malaysia (MOE), Universiti Teknologi Malaysia (UTM), Faculty of Mechanical Engineering, Institute for Vehicle Systems and Engineering and UTM Centre for Low Carbon Transport in cooperation with Imperial College London for providing the research facilities. This research work has been supported by Ministry of Education Malaysia (MOE) for the FRGS Grant (R.J130000.7824.4F723).

## Appendix A. Supplementary material

Supplementary data associated with this article can be found, in the online version, at <http://dx.doi.org/10.1016/j.cossms.2017.08.002>.

## References

- [1] S. Zhang, H. Miyanaji, L. Yanga, A. Ali, J.J.S. Dilipa, Brent, An experimental study of ceramic dental porcelain materials using A 3D Print (3DP) process, in: Proceeding of Solid Freeform Fabrication (SFF) Symposium, 2014, pp.991–1011.
- [2] A. Withell, O. Diegel, I. Grupp, S. Reay, D. de Beer, J. Potgieter, Porous ceramic filters through 3D printing, in: Innovative Developments in Virtual and Physical Prototyping: Proceedings of the 5th International Conference on Advanced Research in Virtual and Rapid Prototyping, Leiria, Portugal, 28 September–1 October, 2011, CRC Press, 2011, pp. 313–318.
- [3] A. Patel, P. Cosman, S. Desai, Three-dimensional Printing Technology in Surgery, 2015.
- [4] T. Zhou, J. Zhu, Application of 3D printing and micro-CT scan to rock dynamics, in: Rock Dynamics: From Research to Engineering: Proceedings of the 2nd International Conference on Rock Dynamics and Applications, CRC Press, 2016, p. 247.
- [5] E. Sachs, M. Cima, J. Cornie, Three-dimensional printing: rapid tooling and prototypes directly from a CAD model, *CIRP Ann. – Manuf. Technol.* 39 (1) (1990) 201–204.
- [6] K. Leong, C. Cheah, C. Chua, Solid freeform fabrication of three-dimensional scaffolds for engineering replacement tissues and organs, *Biomaterials* 24 (13) (2003) 2363–2378.

- [7] A. Joe Lopes, E. MacDonald, R.B. Wicker, Integrating stereolithography and direct print technologies for 3D structural electronics fabrication, *Rapid Prototyping J.* 18 (2) (2012) 129–143.
- [8] O. Diegel, A. Withell, D. de Beer, J. Potgieter, F. Noble, Low-cost 3D printing of controlled porosity ceramic parts, *Int. J. Automat. Technol.* 6 (5) (2012) 618–626.
- [9] F.-Z. Zhang, T. Kato, M. Fuji, M. Takahashi, Gelcasting fabrication of porous ceramics using a continuous process, *J. Eur. Ceram. Soc.* 26 (4–5) (2006) 667–671.
- [10] T. Chu, K. Szczepkowski, W. Wagner, J. Halloran, Experimental ceramic suspensions for StereoLithography processing of implants, *J. Dent. Res.* (1996) 3046.
- [11] H. Giberti, M. Strano, M. Annoni, An innovative machine for Fused Deposition Modeling of metals and advanced ceramics, in: MATEC Web of Conferences, EDP Sciences, 2016.
- [12] A. Khalyfa, S. Vogt, J. Weisser, G. Grimm, A. Rechtenbach, W. Meyer, M. Schnabelrauch, Development of a new calcium phosphate powder-binder system for the 3D printing of patient specific implants, *J. Mater. Sci. - Mater. Med.* 18 (5) (2007) 909–916.
- [13] H. Shao, Y. He, J. Fu, D. He, X. Yang, J. Xie, C. Yao, J. Ye, S. Xu, Z. Gou, 3D printing magnesium-doped wollastonite/β-TCP bioceramics scaffolds with high strength and adjustable degradation, *J. Eur. Ceram. Soc.* 36 (6) (2016) 1495–1503.
- [14] C. Wu, Y. Luo, G. Cuniberti, Y. Xiao, M. Gelinsky, Three-dimensional printing of hierarchical and tough mesoporous bioactive glass scaffolds with a controllable pore architecture, excellent mechanical strength and mineralization ability, *Acta Biomater.* 7 (6) (2011) 2644–2650.
- [15] C.X.F. Lam, X.M. Mo, S.H. Teoh, D.W. Hutmacher, Scaffold development using 3D printing with a starch-based polymer, *Mater. Sci. Eng., C* 20 (1–2) (2002) 49–56.
- [16] D.W. Hutmacher, Scaffolds in tissue engineering bone and cartilage, *Biomaterials* 21 (24) (2000) 2529–2543.
- [17] H. Seitz, W. Rieder, S. Irsen, B. Leukers, C. Tille, Three-dimensional printing of porous ceramic scaffolds for bone tissue engineering, *J. Biomed. Mater. Res. Part B: Appl. Biomater.* 74 (2) (2005) 782–788.
- [18] G. Brooks, K. Kim, O. Tim, 3D printing as a consumer technology business model, *Int. J. Manage. Inform. Syst. (IJMIS)* 18 (4) (2014) 271–280.
- [19] R. Detsch, S. Schaefer, U. Deisinger, G. Ziegler, H. Seitz, B. Leukers, In vitro-osteoclastic activity studies on surfaces of 3D printed calcium phosphate scaffolds, *J. Biomater. Appl.* (2010).
- [20] P.F. Jacobs, Rapid Prototyping & Manufacturing: Fundamentals of Stereolithography, Society of Manufacturing Engineers, 1992.
- [21] C. Bergmann, M. Lindner, W. Zhang, K. Koczur, A. Kirsten, R. Telle, H. Fischer, 3D printing of bone substitute implants using calcium phosphate and bioactive glasses, *J. Eur. Ceram. Soc.* 30 (12) (2010) 2563–2567.
- [22] C. Mota, D. Puppi, F. Chiellini, E. Chiellini, Additive manufacturing techniques for the production of tissue engineering constructs, *J. Tissue Eng. Regener. Med.* 9 (3) (2015) 174–190.
- [23] A. Farzadi, M. Solati-Hashjin, M. Asadi-Eydivand, N.A.A. Osman, Effect of layer thickness and printing orientation on mechanical properties and dimensional accuracy of 3D printed porous samples for bone tissue engineering, *PLoS one* 9 (9) (2014) e108252.
- [24] I.J. Petrick, T.W. Simpson, 3D printing disrupts manufacturing: how economies of one create new rules of competition, *Res.-Technol. Manage.* 56 (6) (2013) 12–16.
- [25] M. Vaezi, H. Seitz, S. Yang, A review on 3D micro-additive manufacturing technologies, *Int. J. Adv. Manuf. Technol.* 67 (5–8) (2013) 1721–1754.
- [26] R. Gauvin, Y.-C. Chen, J.W. Lee, P. Soman, P. Zorlutuna, J.W. Nichol, H. Bae, S. Chen, A. Khademhosseini, Microfabrication of complex porous tissue engineering scaffolds using 3D projection stereolithography, *Biomaterials* 33 (15) (2012) 3824–3834.
- [27] T. Campbell, C. Williams, O. Ivanova, B. Garrett, Could 3D Printing Change the World, Technologies, Potential, and Implications of Additive Manufacturing, Atlantic Council, Washington, DC, 2011, pp. 1–15.
- [28] T.A. Campbell, O.S. Ivanova, 3D printing of multifunctional nanocomposites, *Nano Today* 8 (2) (2013) 119–120.
- [29] B.C. Gross, J.L. Erkal, S.Y. Lockwood, C. Chen, D.M. Spence, Evaluation of 3D printing and its potential impact on biotechnology and the chemical sciences, *Anal. Chem.* 86 (7) (2014) 3240–3253.
- [30] M.L. Griffith, J.W. Halloran, Freeform fabrication of ceramics via stereolithography, *J. Am. Ceram. Soc.* 79 (10) (1996) 2601–2608.
- [31] W. Yeong, N. Sudarmadji, H. Yu, C. Chua, K. Leong, S. Venkatraman, Y. Boey, L. Tan, Porous polycaprolactone scaffold for cardiac tissue engineering fabricated by selective laser sintering, *Acta Biomater.* 6 (6) (2010) 2028–2034.
- [32] H. Yves-Christian, W. Jan, M. Wilhelm, W. Konrad, P. Reinhart, Net shaped high performance oxide ceramic parts by selective laser melting, *Phys. Procedia* 5 (2010) 587–594.
- [33] N. Fan, W. Wei, B. Liu, A. Wang, R. Luo, Ceramic feedstocks for additive manufacturing, in: 2016 IEEE International Conference on Industrial Technology (ICIT), IEEE, 2016, pp. 1147–1151.
- [34] D.T. Pham, R.S. Gault, A comparison of rapid prototyping technologies, *Int. J. Mach. Tools Manuf.* 38 (10) (1998) 1257–1287.
- [35] R. Melcher, N. Travitzky, C. Zollfrank, P. Greil, 3D printing of Al<sub>2</sub>O<sub>3</sub>/Cu–O interpenetrating phase composite, *J. Mater. Sci.* 46 (5) (2011) 1203–1210.
- [36] J. Ebert, E. Özkel, A. Zeichner, K. Uibel, Ö. Weiss, U. Koops, R. Telle, H. Fischer, Direct inkjet printing of dental prostheses made of zirconia, *J. Dental Res.* 88 (7) (2009) 673–676.
- [37] B. Nan, X. Yin, L. Zhang, L. Cheng, Three-dimensional printing of Ti<sub>3</sub>SiC<sub>2</sub>-based ceramics, *J. Am. Ceram. Soc.* 94 (4) (2011) 969–972.
- [38] X. Yin, N. Travitzky, P. Greil, Three-dimensional printing of nanolaminated Ti<sub>2</sub>AlC<sub>2</sub> toughened TiAl<sub>3</sub>–Al<sub>2</sub>O<sub>3</sub> composites, *J. Am. Ceram. Soc.* 90 (7) (2007) 2128–2134.
- [39] A. Zocca, C.M. Gomes, E. Bernardo, R. Müller, J. Günster, P. Colombo, LAS glass-ceramic scaffolds by three-dimensional printing, *J. Eur. Ceram. Soc.* 33 (9) (2013) 1525–1533.
- [40] H. Zhao, C. Ye, Z. Fan, Y. Shi, 3D Printing of ZrO<sub>2</sub> Ceramic using Nano-zirconia Suspension as a Binder, 2016.
- [41] C.G. Mançanares, E.d.S. Zancul, J.C. da Silva, P.A.C. Miguel, Additive manufacturing process selection based on parts' selection criteria, *Int. J. Adv. Manuf. Technol.* 80 (5–8) (2015) 1007–1014.
- [42] J.W. Lee, G. Ahn, D.S. Kim, D.-W. Cho, Development of nano-and microscale composite 3D scaffolds using PPF/DEF-HA and micro-stereolithography, *Microelectron. Eng.* 86 (4) (2009) 1465–1467.
- [43] C. Provin, S. Monneret, Complex ceramic-polymer composite microparts made by microstereolithography, *IEEE Trans. Electron. Packag. Manuf.* 25 (1) (2002) 59–63.
- [44] V. Popov, A. Evseev, A. Ivanov, V. Roginski, A. Volozhin, S. Howdle, Laser stereolithography and supercritical fluid processing for custom-designed implant fabrication, *J. Mater. Sci. - Mater. Med.* 15 (2) (2004) 123–128.
- [45] C. Hinczewski, S. Corbel, T. Chartier, Ceramic suspensions suitable for stereolithography, *J. Eur. Ceram. Soc.* 18 (6) (1998) 583–590.
- [46] A. Licciulli, C.E. Corcione, A. Greco, V. Amicarelli, A. Maffezzoli, Laser stereolithography of ZrO<sub>2</sub> toughened Al<sub>2</sub>O<sub>3</sub>, *J. Eur. Ceram. Soc.* 25 (9) (2005) 1581–1589.
- [47] T.-M.G. Chu, D.G. Orton, S.J. Hollister, S.E. Feinberg, J.W. Halloran, Mechanical and in vivo performance of hydroxyapatite implants with controlled architectures, *Biomaterials* 23 (5) (2002) 1283–1293.
- [48] C. Chaput, T. Chartier, Fabrication of ceramics by Stereolithography, RTejournal-Forum für Rapid Technologie, 2007, p. 1.
- [49] F.P. Melchels, J. Feijen, D.W. Grijpma, A review on stereolithography and its applications in biomedical engineering, *Biomaterials* 31 (24) (2010) 6121–6130.
- [50] P.S. D'Urso, D.J. Effeney, W.J. Earwaker, T.M. Barker, M.J. Redmond, R.G. Thompson, F.H. Tomlinson, Custom cranioplasty using stereolithography and acrylic, *Br. J. Plast. Surg.* 53 (3) (2000) 200–204.
- [51] D.P. Sarment, P. Sukovic, N. Clinthrope, Accuracy of implant placement with a stereolithographic surgical guide, *Int. J. Oral Maxillofac. Implants* 18 (4) (2003).
- [52] E. Zanchetta, M. Cattaldo, G. Franchin, M. Schwentenwein, J. Homa, G. Brusatin, P. Colombo, Stereolithography of SiOC ceramic microcomponents, *Adv. Mater.* 28 (2) (2016) 370–376.
- [53] M. Schwentenwein, J. Homa, Additive manufacturing of dense alumina ceramics, *Int. J. Appl. Ceram. Technol.* 12 (1) (2015) 1–7.
- [54] H.N. Chia, B.M. Wu, Recent advances in 3D printing of biomaterials, *J. Biol. Eng.* 9 (1) (2015) 1–14.
- [55] X. Zhang, X. Jiang, C. Sun, Micro-stereolithography of polymeric and ceramic microstructures, *Sens. Actuators, A* 77 (2) (1999) 149–156.
- [56] K. Wu, J. Halloran, Photopolymerization monitoring of ceramic stereolithography resins by FTIR methods, *J. Mater. Sci.* 40 (1) (2005) 71–76.
- [57] S. Tasaki, S. Kirihara, T. Soumura, Fabrication of ceramic dental crowns by using stereolithography and powder sintering process, in: Ceramic Engineering and Science Proceedings, American Ceramic Society, Inc., 735 Ceramic Place Westerville OH 43081 United States, 2011, pp. 141–146.
- [58] K.-S. Lee, R.H. Kim, D.-Y. Yang, S.H. Park, Advances in 3D nano/microfabrication using two-photon initiated polymerization, *Prog. Polym. Sci.* 33 (6) (2008) 631–681.
- [59] T. Weiß, G. Hildebrand, R. Schade, K. Liefelth, Two-photon polymerization for microfabrication of three-dimensional scaffolds for tissue engineering application, *Eng. Life Sci.* 9 (5) (2009) 384–390.
- [60] J. Hyuk Moon, S. Yang, Creating three-dimensional polymeric microstructures by multi-beam interference lithography, *J. Macromol. Sci., Part C: Polymer Rev.* 45 (4) (2005) 351–373.
- [61] A.M. Prenen, J. Van Der Werf, C.W. Bastiaansen, D.J. Broer, Monodisperse, polymeric nano-and microsieves produced with interference holography, *Adv. Mater.* 21 (17) (2009) 1751–1755.
- [62] F.P. Melchels, K. Bertoldi, R. Gabbielli, A.H. Velders, J. Feijen, D.W. Grijpma, Mathematically defined tissue engineering scaffold architectures prepared by stereolithography, *Biomaterials* 31 (27) (2010) 6909–6916.
- [63] L.E. Criales, Y.M. Arisoy, T. Öznel, Sensitivity analysis of material and process parameters in finite element modeling of selective laser melting of Inconel 625, *Int. J. Adv. Manuf. Technol.* (2016) 1–14.
- [64] S. Rüsenberg, L. Schmidt, H. Hosse, H.J. Schmid, Porosity as a key to increase material properties of laser sintered parts, *Innovative Developments in Virtual and Physical Prototyping*, CRC Press, 2011, pp. 531–538.
- [65] Y. Xia, P. Zhou, X. Cheng, Y. Xie, C. Liang, C. Li, S. Xu, Selective laser sintering fabrication of nano-hydroxyapatite/poly-e-caprolactone scaffolds for bone tissue engineering applications, *Int. J. Nanomed.* 8 (2013) 4197.
- [66] S. Das, Selective laser sintering of polymers and polymer-ceramic composites, *Virtual Prototyping Bio Manuf. Med. Appl.* (2008) 226–260.

- [67] K. Tan, C. Chua, K. Leong, C. Cheah, W. Gui, W. Tan, F. Wiria, Selective laser sintering of biocompatible polymers for applications in tissue engineering, *Bio-medical Mater. Eng.* 15 (1,2) (2005) 113–124.
- [68] D.N. Silva, M.G. De Oliveira, E. Meurer, M.I. Meurer, J.V.L. da Silva, A. Santa-Bárbara, Dimensional error in selective laser sintering and 3D-printing of models for craniomaxillary anatomy reconstruction, *J. Cranio Maxillofac. Surg.* 36 (8) (2008) 443–449.
- [69] A. Ridwan-Pramana, P. Marcián, L. Borák, N. Narra, T. Forouzanfar, J. Wolff, Structural and mechanical implications of PMMA implant shape and interface geometry in cranioplasty – a finite element study, *J. Cranio Maxillofac. Surg.* 44 (1) (2016) 34–44.
- [70] F. Rengier, A. Mehndiratta, H. von Tengg-Kobligk, C.M. Zechmann, R. Unterhinninghofen, H.-U. Kauczor, F.L. Giesel, 3D printing based on imaging data: review of medical applications, *Int. J. Comput. Assist. Radiol. Surg.* 5 (4) (2010) 335–341.
- [71] Y. Hagedorn, N. Balachandran, W. Meiners, K. Wissenbach, R. Poprawe, SLM of net-shaped high strength ceramics: new opportunities for producing dental restorations, in: Proceedings of the Solid Freeform Fabrication Symposium, Austin, TX, Aug, 2011, pp. 8–10.
- [72] J. Wilkes, Y.-C. Hagedorn, S. Ocylok, W. Meiners, K. Wissenbach, Rapid manufacturing of ceramic parts by selective laser melting, in: Ceramic Engineering and Science Proceedings, Wiley-Blackwell, 111 River Street Hoboken NJ 07030-5774 United States, 2010, p. 137.
- [73] G. Brunello, S. Sivolella, R. Meneghelli, L. Ferroni, C. Gardin, A. Piattelli, B. Zavan, E. Bressan, Powder-based 3D printing for bone tissue engineering, *Biotechnol. Adv.* (2016).
- [74] I. Zein, D.W. Hutmacher, K.C. Tan, S.H. Teoh, Fused deposition modeling of novel scaffold architectures for tissue engineering applications, *Biomaterials* 23 (2002).
- [75] S. Mohanty, L.B. Larsen, J. Trifol, P. Szabo, H.V.R. Burri, C. Canali, M. Dufva, J. Emnéus, A. Wolff, Fabrication of scalable and structured tissue engineering scaffolds using water dissolvable sacrificial 3D printed moulds, *Mater. Sci. Eng., C* 55 (2015) 569–578.
- [76] B.G. Compton, J.A. Lewis, 3D-printing of lightweight cellular composites, *Adv. Mater.* 26 (34) (2014) 5930–5935.
- [77] S. Onagoruwa, S. Bose, A. Bandyopadhyay, Fused deposition of ceramics (FDC) and composites, *Pre-SFF*, Texas, 2001, 224–31.
- [78] N. Xu, X. Ye, D. Wei, J. Zhong, Y. Chen, G. Xu, D. He, 3D artificial bones for bone repair prepared by computed tomography-guided fused deposition modeling for bone repair, *ACS Appl. Mater. Interfaces* 6 (17) (2014) 14952–14963.
- [79] T.-L.B. Tseng, A. Chilukuri, S.C. Park, Y.J. Kwon, Automated quality characterization of 3D printed bone scaffolds, *J. Comput. Des. Eng.* 1 (3) (2014) 194–201.
- [80] T. McNulty, F. Mohammadi, A. Bandyopadhyay, D. Shanefield, S. Danforth, A. Safari, Development of a binder formulation for fused deposition of ceramics, *Rapid Prototyping J.* 4 (4) (1998) 144–150.
- [81] A. Bandyopadhyay, R. Panda, T. McNulty, F. Mohammadi, S. Danforth, A. Safari, Piezoelectric ceramics and composites via rapid prototyping techniques, *Rapid Prototyping J.* 4 (1) (1998) 37–49.
- [82] A. Bandyopadhyay, R.K. Panda, V.F. Janas, M.K. Agarwala, S.C. Danforth, A. Safari, Processing of piezocomposites by fused deposition technique, *J. Am. Ceram. Soc.* 80 (6) (1997) 1366–1372.
- [83] M. Agarwala, A. Bandyopadhyay, R. Van Weeren, N. Langrana, A. Safari, S. Danforth, Fused deposition of ceramics (FDC) for structural silicon nitride components, *Solid Freeform Fabr. Proc.* (1996) 335–344.
- [84] M. Jafari, W. Han, F. Mohammadi, A. Safari, S. Danforth, N. Langrana, A novel system for fused deposition of advanced multiple ceramics, *Rapid Prototyping J.* 6 (3) (2000) 161–175.
- [85] J.P. Li, J.R. de Wijn, C.A. Van Blitterswijk, K. de Groot, Porous Ti 6 Al 4 V scaffold directly fabricating by rapid prototyping: preparation and in vitro experiment, *Biomaterials* 27 (8) (2006) 1223–1235.
- [86] J.A. Inzana, D. Olvera, S.M. Fuller, J.P. Kelly, O.A. Graeve, E.M. Schwarz, Kates L. Stephen, H.A. Awad, 3D printing of composite calcium phosphate and collagen scaffolds for bone regeneration, *Biomaterials* 35 (13) (2014) 4026–4034.
- [87] B. Leukers, H. Gülkán, S.H. Irsen, S. Milz, C. Tille, M. Schieker, H. Seitz, Hydroxyapatite scaffolds for bone tissue engineering made by 3D printing, *J. Mater. Sci. - Mater. Med.* 16 (12) (2005) 1121–1124.
- [88] Y. Wang, X. Li, Q. Wei, M. Yang, S. Wei, Study on the mechanical properties of three-dimensional directly binding hydroxyapatite powder, *Cell Biochem. Biophys.* 72 (1) (2015) 289–295.
- [89] Y. Wang, Q. Wei, F. Pan, M. Yang, S. Wei, Molecular dynamics simulations for the examination of mechanical properties of hydroxyapatite/poly  $\alpha$ -n-butyl cyanoacrylate under additive manufacturing, *Bio-Med. Mater. Eng.* 24 (1) (2014) 825–833.
- [90] Q. Wei, Y. Wang, X. Li, M. Yang, W. Chai, K. Wang, Y. Zhang, Study the bonding mechanism of binders on hydroxyapatite surface and mechanical properties for 3DP fabrication bone scaffolds, *J. Mech. Behav. Biomed. Mater.* 57 (2016) 190–200.
- [91] S.C. Cox, J.A. Thornby, G.J. Gibbons, M.A. Williams, K.K. Mallick, 3D printing of porous hydroxyapatite scaffolds intended for use in bone tissue engineering applications, *Mater. Sci. Eng., C* 47 (2015) 237–247.
- [92] Z. Zhou, F. Buchanan, C. Mitchell, N. Dunne, Printability of calcium phosphate: calcium sulfate powders for the application of tissue engineered bone scaffolds using the 3D printing technique, *Mater. Sci. Eng., C* 38 (2014) 1–10.
- [93] L. Strobel, S. Rath, A. Maier, J. Beier, A. Arkudas, P. Greil, R. Horch, U. Kneser, Induction of bone formation in biphasic calcium phosphate scaffolds by bone morphogenetic protein-2 and primary osteoblasts, *J. Tissue Eng. Regener. Med.* 8 (3) (2014) 176–185.
- [94] P.H. Warnke, H. Seitz, F. Warnke, S.T. Becker, S. Sivananthan, E. Sherry, Q. Liu, J. Wiltfang, T. Douglas, Ceramic scaffolds produced by computer-assisted 3D printing and sintering: characterization and biocompatibility investigations, *J. Biomed. Mater. Res. B Appl. Biomater.* 93 (1) (2010) 212–217.
- [95] A. Butscher, M. Bohner, N. Doeblin, S. Hofmann, R. Müller, New depowdering-friendly designs for three-dimensional printing of calcium phosphate bone substitutes, *Acta Biomater.* 9 (11) (2013) 9149–9158.
- [96] S. Tarafder, W.S. Dernell, A. Bandyopadhyay, S. Bose, SrO-and MgO-doped microwave sintered 3D printed tricalcium phosphate scaffolds: Mechanical properties and in vivo osteogenesis in a rabbit model, *J. Biomed. Mater. Res. B Appl. Biomater.* 103 (3) (2015) 679–690.
- [97] S. Tarafder, N. Davies, A. Bandyopadhyay, 3D printed tricalcium phosphate scaffolds: effect of SrO and MgO doping on in vivo osteogenesis in a rat distal femoral defect model, *Biomater.* 32 (2013) 1250–1259.
- [98] G. Fielding, S. Bose, SiO<sub>2</sub> and ZnO dopants in three-dimensionally printed tricalcium phosphate bone tissue engineering scaffolds enhance osteogenesis and angiogenesis in vivo, *Acta Biomater.* 9 (11) (2013) 9137–9148.
- [99] F. Tamimi, J. Torres, K. Al-Abdalla, E. Lopez-Cabarcos, M.H. Alkhraisat, D.C. Bassett, U. Gbureck, J.E. Barralet, Osseointegration of dental implants in 3D-printed synthetic onlay grafts customized according to bone metabolic activity in recipient site, *Biomaterials* 35 (21) (2014) 5436–5445.
- [100] J. Torres, F. Tamimi, M.H. Alkhraisat, J.C. Prados-Frutos, E. Rastikerdar, U. Gbureck, J.E. Barralet, E. López-Cabarcos, Vertical bone augmentation with 3D-synthetic monetite blocks in the rabbit calvaria, *J. Clin. Periodontol.* 38 (12) (2011) 1147–1153.
- [101] S. Tarafder, V.K. Balla, N.M. Davies, A. Bandyopadhyay, S. Bose, Microwave-sintered 3D printed tricalcium phosphate scaffolds for bone tissue engineering, *J. Tissue Eng. Regener. Med.* 7 (8) (2013) 631–641.
- [102] U. Klammert, U. Gbureck, E. Vorndran, J. Rödiger, P. Meyer-Marcotty, A.C. Kübler, 3D powder printed calcium phosphate implants for reconstruction of cranial and maxillofacial defects, *J. Cranio-Maxillofac. Surg.* 38 (8) (2010) 565–570.
- [103] M. Castilho, M. Dias, U. Gbureck, J. Groll, P. Fernandes, I. Pires, B. Gouveia, J. Rodrigues, E. Vorndran, Fabrication of computationally designed scaffolds by low temperature 3D printing, *Biofabrication* 5 (3) (2013) 035012.
- [104] M. Castilho, M. Dias, E. Vorndran, U. Gbureck, P. Fernandes, I. Pires, B. Gouveia, H. Armés, E. Pires, J. Rodrigues, Application of a 3D printed customized implant for canine cruciate ligament treatment by tibial tuberosity advancement, *Biofabrication* 6 (2) (2014) 025005.
- [105] M. Castilho, C. Moseke, A. Ewald, Direct 3D powder printing of biphasic calcium phosphate scaffolds for substitution of complex bone defects, *Biofabrication* 6 (1) (2014) 015006.
- [106] U. Klammert, E. Vorndran, T. Reuther, F.A. Müller, K. Zorn, U. Gbureck, Low temperature fabrication of magnesium phosphate cement scaffolds by 3D powder printing, *J. Mater. Sci.: Mater. Med.* 21 (11) (2010) 2947–2953.
- [107] M. Lipowiecki, M. Ryvolova, Á. Töttösi, N. Kolmer, S. Naher, S.A. Brennan, M. Vazquez, D. Brabazon, Permeability of rapid prototyped artificial bone scaffold structures, *J. Biomed. Mater. Res., Part A* 102 (11) (2014) 4127–4135.
- [108] F.-H. Liu, Y.-K. Shen, J.-L. Lee, Selective laser sintering of a hydroxyapatite-silica scaffold on cultured MG63 osteoblasts in vitro, *Int. J. Precis. Eng. Manuf.* 13 (3) (2012) 439–444.
- [109] G. Wang, Z. Lu, D. Dwarthe, H. Zreiqat, Porous scaffolds with tailored reactivity modulate in-vitro osteoblast responses, *Mater. Sci. Eng., C* 32 (7) (2012) 1818–1826.
- [110] H.-C. Yen, A new slurry-based shaping process for fabricating ceramic green part by selective laser scanning the gelled layer, *J. Eur. Ceram. Soc.* 32 (12) (2012) 3123–3128.
- [111] F.-H. Liu, Synthesis of biomedical composite scaffolds by laser sintering: mechanical properties and in vitro bioactivity evaluation, *Appl. Surf. Sci.* 297 (2014) 1–8.
- [112] A. Butscher, M. Bohner, C. Roth, A. Ernstberger, R. Heuberger, N. Doeblin, P.R. Von Rohr, R. Müller, Printability of calcium phosphate powders for three-dimensional printing of tissue engineering scaffolds, *Acta Biomater.* 8 (1) (2012) 373–385.
- [113] C. Wu, J. Chang, W. Zhai, S. Ni, A novel bioactive porous bredigite (Ca<sub>7</sub>MgSi<sub>4</sub>O<sub>16</sub>) scaffold with biomimetic apatite layer for bone tissue engineering, *J. Mater. Sci. - Mater. Med.* 18 (5) (2007) 857–864.
- [114] Q.Z. Chen, I.D. Thompson, A.R. Boccaccini, 4555 Bioglass®-derived glass-ceramic scaffolds for bone tissue engineering, *Biomaterials* 27 (11) (2006) 2414–2425.
- [115] G. Heim, Advanced ceramics for biomedical applications, *Angew. Chem., Int. Ed. Engl.* 28 (1) (1989) 111–116.
- [116] S. Bose, S. Vahabzadeh, A. Bandyopadhyay, Bone tissue engineering using 3D printing, *Mater. Today* 16 (12) (2013) 496–504.
- [117] G.A. Fielding, A. Bandyopadhyay, S. Bose, Effects of SiO<sub>2</sub> and ZnO doping on mechanical and biological properties of 3D printed TCP scaffolds, *Dent. Mater.* 28 (2) (2012) 113–122.
- [118] A.L. Torres, V.M. Gaspar, I.R. Serra, G.S. Diogo, R. Fradique, A.P. Silva, I.J. Correia, Bioactive polymeric-ceramic hybrid 3D scaffold for application in bone tissue regeneration, *Mater. Sci. Eng., C* 33 (7) (2013) 4460–4469.
- [119] F.T. Zohora, A.Y.M.A. Azim, Biomaterials as porous scaffolds for tissue engineering applications: a review, *Eur. Sci. J.* 10 (21) (2014).

- [120] C.-H. Chang, C.-Y. Lin, F.-H. Liu, M.H.-C. Chen, C.-P. Lin, H.-N. Ho, Y.-S. Liao, 3D printing bioceramic porous scaffolds with good mechanical property and cell affinity, *PLoS one* 10 (11) (2015) e0143713.
- [121] X. Chen, B. Lei, Y. Wang, N. Zhao, Morphological control and in vitro bioactivity of nanoscale bioactive glasses, *J. Non-Cryst. Solids* 355 (13) (2009) 791–796.
- [122] L.Z. Yang, S.G. Oliveira, B. Stuckera, Development of a 3D printing method for production of dental application, in: Proceedings of the 24th International Solid Freeform Fabrication Symposium, Austin, TX, USA, 2013, pp. 346–353.
- [123] J. Yoo, M.J. Cima, S. Khanuja, E.M. Sachs, Structural ceramic components by 3D printing, in: Solid Freeform Fabrication Symposium, DTIC Document, 1993, pp. 40–50.
- [124] S. Spath, P. Drescher, H. Seitz, Impact of particle size of ceramic granule blends on mechanical strength and porosity of 3D printed scaffolds, *Materials* 8 (8) (2015) 4720–4732.
- [125] C.F. Santos, A.P. Silva, L. Lopes, I. Pires, I.J. Correia, Design and production of sintered  $\beta$ -tricalcium phosphate 3D scaffolds for bone tissue regeneration, *Mater. Sci. Eng., C* 32 (5) (2012) 1293–1298.
- [126] U. Gbureck, T. Hözel, U. Klammert, K. Würzler, F.A. Müller, J.E. Barralet, Resorbable dicalcium phosphate bone substitutes prepared by 3D powder printing, *Adv. Func. Mater.* 17 (18) (2007) 3940–3945.
- [127] A. Kumar, S. Mandal, S. Barui, R. Vasireddi, U. Gbureck, M. Gelinsky, B. Basu, Low temperature additive manufacturing of three dimensional scaffolds for bone-tissue engineering applications: processing related challenges and property assessment, *Mater. Sci. Eng.: R: Rep.* 103 (2016) 1–39.
- [128] M. Asadi-Eydivand, M. Solati-Hashjin, A. Fathi, M. Padashi, N.A.A. Osman, Optimal design of a 3D-printed scaffold using intelligent evolutionary algorithms, *Appl. Soft Comput.* 39 (2016) 36–47.
- [129] A. Tiwari, M.R. Alenezi, S.C. Jun, Advanced Composite Materials, John Wiley & Sons, 2016.
- [130] E. Vordran, C. Moseke, U. Gbureck, 3D printing of ceramic implants, *MRS Bull.* 40 (02) (2015) 127–136.
- [131] R.M. German, Handbook of Mathematical Relations in Particulate Materials Processing, John Wiley & Sons, 2009.
- [132] R. Chumnanklang, T. Panyathanmaporn, K. Sitthiseripratip, J. Suwanprateeb, 3D printing of hydroxyapatite: effect of binder concentration in pre-coated particle on part strength, *Mater. Sci. Eng., C* 27 (4) (2007) 914–921.
- [133] M.B. Uday, M.N. Ahmad-Fauzi, Alias Mohd Noor, S. Rajoo, Current issues and problems in the joining of ceramic to metal, Ch.8, in: Joining Technologies, InTech, 2016, pp. 159–193.
- [134] S. Amirkhani, R. Bagheri, A. Zehtab Yazdi, Effect of pore geometry and loading direction on deformation mechanism of rapid prototyped scaffolds, *Acta Mater.* 60 (6–7) (2012) 2778–2789.
- [135] S.A. Uhland, R.K. Holman, S. Morissette, M.J. Cima, E.M. Sachs, Strength of green ceramics with low binder content, *J. Am. Ceram. Soc.* 84 (12) (2001) 2809–2818.
- [136] A. Butscher, M. Bohner, S. Hofmann, L. Gauckler, R. Müller, Structural and material approaches to bone tissue engineering in powder-based three-dimensional printing, *Acta Biomater.* 7 (3) (2011) 907–920.
- [137] M.G. Li, X.Y. Tian, X.B. Chen, Modeling of flow rate, pore size, and porosity for the dispensing-based tissue scaffolds fabrication, *J. Manuf. Sci. Eng.* 131 (3) (2009). 034501–034501.
- [138] S. Bose, M. Roy, A. Bandyopadhyay, Recent advances in bone tissue engineering scaffolds, *Trends Biotechnol.* 30 (10) (2012) 546–554.
- [139] C. Wu, W. Zhou, Y. Luo, M. Gelinsky, J. Chang, Y. Xiao, 3D-printing of highly uniform  $\text{CaSiO}_3$  ceramic scaffolds: preparation, characterization and in vivo osteogenesis, *J. Mater. Chem.* 22 (24) (2012) 12288–12295.
- [140] S. Yang, K.-F. Leong, Z. Du, C.-K. Chua, The design of scaffolds for use in tissue engineering. Part I. Traditional factors, *Tissue Eng.* 7 (6) (2001) 679–689.
- [141] S.J. Hollister, Porous scaffold design for tissue engineering, *Nat. Mater.* 4 (7) (2005) 518–524.
- [142] E.N. Antonov, V.N. Bagratashvili, M.J. Whitaker, J.J. Barry, K.M. Shakesheff, A. N. Konovalov, V.K. Popov, S.M. Howdle, Three-dimensional bioactive and biodegradable scaffolds fabricated by surface-selective laser sintering, *Adv. Mater.* 17 (3) (2005) 327–330.
- [143] X. Liu, P.X. Ma, Polymeric scaffolds for bone tissue engineering, *Ann. Biomed. Eng.* 32 (3) (2004) 477–486.
- [144] V. Karageorgiou, D. Kaplan, Porosity of 3D biomaterial scaffolds and osteogenesis, *Biomaterials* 26 (27) (2005) 5474–5491.
- [145] J. Suwanprateeb, R. Sanngam, W. Suwanpruk, T. Panyathanmaporn, Mechanical and in vitro performance of apatite–wollastonite glass ceramic reinforced hydroxyapatite composite fabricated by 3D-printing, *J. Mater. Sci. - Mater. Med.* 20 (6) (2009) 1281–1289.
- [146] J. Suwanprateeb, R. Sanngam, W. Suwanpruk, Fabrication of bioactive hydroxyapatite/bis-GMA based composite via three dimensional printing, *J. Mater. Sci. - Mater. Med.* 19 (7) (2008) 2637–2645.